

Summer 6-15-2017

# Design and Implementation of a Microscope Based on Magneto-Optic Effects

Yuxuan Liu

Rose-Hulman Institute of Technology, liuy8@rose-hulman.edu

Follow this and additional works at: [http://scholar.rose-hulman.edu/dept\\_optics](http://scholar.rose-hulman.edu/dept_optics)



Part of the [Optics Commons](#)

---

## Recommended Citation

Liu, Yuxuan, "Design and Implementation of a Microscope Based on Magneto-Optic Effects" (2017). *Graduate Theses - Physics and Optical Engineering*. 1.

[http://scholar.rose-hulman.edu/dept\\_optics/1](http://scholar.rose-hulman.edu/dept_optics/1)

This Thesis is brought to you for free and open access by the Physics and Optical Engineering at Rose-Hulman Scholar. It has been accepted for inclusion in Graduate Theses - Physics and Optical Engineering by an authorized administrator of Rose-Hulman Scholar. For more information, please contact [weir1@rose-hulman.edu](mailto:weir1@rose-hulman.edu).

# **Design and Implementation of a Microscope Based on Magneto-Optic Effects**

by

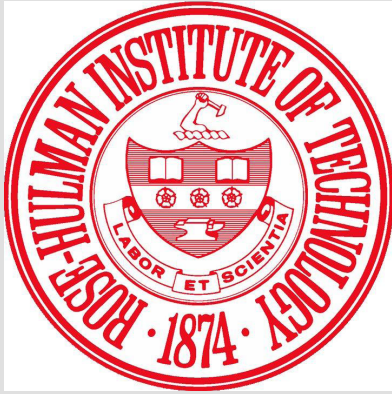
Yuxuan Liu<sup>©</sup>

Advisor: Dr. Maarij Syed

Physics and Optical Engineering Department

Rose-Hulman Institute of Technology

June, 2017



**ROSE-HULMAN INSTITUTE OF TECHNOLOGY**

**Final Examination Report**

Name \_\_\_\_\_

Graduate Major \_\_\_\_\_

Thesis Title \_\_\_\_\_

**DATE OF EXAM:**

**EXAMINATION COMMITTEE:**

<b>Thesis Advisory Committee</b>	<b>Department</b>
Thesis Advisor:	

**PASSED** \_\_\_\_\_

**FAILED** \_\_\_\_\_

## **ABSTRACT**

When light passes through a medium that is subjected to a strong magnetic field, its polarization state may change due to magneto-optic effects such as Faraday rotation. An imaging system based on this polarization change is designed and constructed. The imaging system is built around a magnetic pulse field generator and able to detect polarization change of the incident light due to magneto-optic effects. An automated scheme is implemented using LabView. The program is developed to integrate all hardware and conduct multiple measurements automatically to enhance sensitivity. Basic testing measurements are conducted to evaluate the performance of the system. A metal film made of 50nm thick nickel and aluminum layer is tested and preliminary results are presented. Apart from the final design and experimental results, problems about laser imaging, system vibration and an early design using simple concave lens are also discussed. While no system can be universally ideal for all kinds of samples, an attempt is made to discuss ideal samples for imaging and how the performance may be affected by other types of samples. Various possible future improvements are also discussed and prioritized.

## **ACKNOWLEDGEMENTS**

The author would like to thank professor Maarij Syed for his patient guidance, enthusiastic encouragement and especially his complete trust in me. He has spent more than enough time with me discussing problems and possibilities of the project and helped me with the revising of this paper. I have learnt a lot from this project and I hope a solid foundation has been paved for the future research.

I am also grateful to professor Richard Liptak and the technician Brain Fair for their help and efforts on the manufacture of thin film targets. They have been spent a lot of time discussing and working with me in the MiNDS lab and I deeply appreciate their help.

Furthermore, I would like to express my appreciation to the department technicians Roger Sladek and Benjamin Webster for their technical support on this project and their help on 3D printing multiple parts for the system. I also want to thank professor Jennifer O'Connor for her help on blood sample preparation.

My special thanks are extended to my parents for their full support during my study and Rose-Hulman Institute of Technology for providing me the opportunity and financial support of this program.

**TABLE OF CONTENT**

CHAPTER 1. INTRODUCTION .....	1
CHAPTER 2. BASIC CONCEPTS INTRODUCTION .....	3
2.1 <u>Faraday Rotation</u> .....	3
2.2 <u>Malus Law</u> .....	4
2.3 <u>Coherence of Light</u> .....	6
2.4 <u>Huygens-Fresnel Principle and Collimated Light</u> .....	9
2.5 <u>Fourier Transform Introduction</u> .....	12
CHAPTER 3. SETUP CONCEPT INTRODUCTION .....	16
CHAPTER 4. PRELIMINARY SETUP DISCUSSION .....	20
4.1 <u>Preliminary Setup Description</u> .....	20
4.2 <u>Problems Encountered in the Preliminary Setup</u> .....	22
CHAPTER 5. FINAL SETUP INTRODUCTION .....	28
5.1 <u>Final Setup Description</u> .....	28
5.2 <u>Problems of Laser Wide-Field Imaging</u> .....	29
CHAPTER 6. FINAL SETUP TESTING .....	32
6.1 <u>Magnetic Field Calibration</u> .....	32

6.2 <u>Water Measurement for System Testing</u> .....	33
6.2 <u>Water Measurement for System Testing</u> .....	33
6.3 <u>Optical Resolution Test</u> .....	35
6.4 <u>Sensitivity Test</u> .....	36
CHAPTER 7. FUTURE WORK .....	40
7.1 <u>Imaging of Liquid and Solid Samples</u> .....	40
7.2 <u>Possible Improvements for the System</u> .....	42
REFERENCE .....	44
APPENDIX 1. FINAL SETUP DETAIL.....	46
APPENDIX 2. PRELIMINARY SETUP DETAIL .....	55
APPENDIX 3. HARDWARE INTEGRATION USING LABVIEW .....	59
APPENDIX 4. MECHANICAL PARTS .....	65
APPENDIX 5. DEPOSITION PROCESS .....	70

## 1. INTRODUCTION

Light can have strong interactions with materials. It can therefore serve as a valuable tool in detecting magnetic properties of the materials. While the list of magnetic phenomena detectable through optical techniques is long established, the interaction utilized in this project is Faraday rotation which results in a change in the polarization state of the light as it interacts with magnetic dipoles or free electrons in the material. By using polarizers, the change in the polarization state can be converted into intensity change which can be easily detected and used to evaluate the magnetic response of the material. However, for certain systems where the magnetic response varies spatially, such as magnetic particles in a liquid system or systems with magnetic domains, the total intensity change is not enough to characterize those systems. Therefore, an imaging technique is needed to collect all information about the spatial variance in magnetic properties. Using Faraday rotation, multiple techniques have been developed to image the magnetic properties of different materials. Some techniques directly detect how the sample rotates a linear-polarized light when illuminated by collimated light<sup>[1][2]</sup>, and others use a Faraday indicator (ferromagnetic garnet film) to visualize the magnetic field near the sample in a reflection geometry<sup>[3][4]</sup>.

The goal of this project is to build an imaging system that exploits Faraday rotation from the sample or any other change in its polarization state which indicates its magnetic properties. Related theoretical concepts are introduced in Chapter 2 to help the reader understand the system principles and problems encountered. The basic concept of the setup is introduced in Chapter 3. A preliminary design is discussed in Chapter 4. Although this design was abandoned, its limitations



and problems are still discussed, given that lessons learned from this attempt help formulate the final design. The detailed explanation about the final setup is described in the Chapter 5 and 6 and discussion about further improvement and samples of interest is included in Chapter 7. More detailed information about the hardware and software of the setup can be found in the appendices.

## 2. BASIC CONCEPTS INTRODUCTION

In this chapter, some background concepts are introduced to help the reader understand the system and the problems encountered. Readers can skip this chapter if they are already familiar with the concepts presented here.

### 2.1 Faraday Rotation

Faraday rotation is an interaction between light and materials where the polarization state of incident light is changed. If the light is linearly polarized before the interaction, the polarization change can be observed as a change of its orientation, so the light is “rotated”. First discovered by Michael Faraday in 1845, Faraday rotation has become a technique to detect interactions between light and magnetic materials.

Faraday rotation occurs when the permittivity or permeability of the material become non-diagonal as shown in the following mathematical forms, (2.1.1) and (2.1.2). This form of permittivity or permeability gives the material an anisotropic constitutive relation which is essential to solve Maxwell equations.

$$\vec{\epsilon} = \begin{pmatrix} \epsilon_1 & i\epsilon_2 & 0 \\ -i\epsilon_2 & \epsilon_1 & 0 \\ 0 & 0 & \epsilon_z \end{pmatrix} \quad (2.1.1)$$

$$\vec{\mu} = \begin{pmatrix} \mu_1 & -i\mu_2 & 0 \\ i\mu_2 & \mu_1 & 0 \\ 0 & 0 & \mu_z \end{pmatrix} \quad (2.1.2)$$

When the incident light is propagating in the  $z$ -axis direction, the two eigenmodes of the Maxwell equations are left- and right-handed circularly polarized light propagating at different speeds through the material, which is a property known as circular birefringence. Since a linearly polarized light can be treated as a superposition of two equal-amplitude circularly polarized components with opposite handedness, the phase difference induced by their different propagation speeds will eventually cause the orientation of the polarization to rotate.

This phenomenon can be seen in materials with certain anisotropic structures. Moreover, external magnetic field can cause this circular birefringence in isotropic materials including liquid such as water due to its effect on the wave function of free electrons<sup>[5]</sup>. In this case, the rotation angle depends on several factors as shown in equation (2.1.3),

$$\theta = BVl \quad (2.1.3)$$

where  $\theta$  is the rotation angle;  $B$  is the amplitude of magnetic field in the propagation direction;  $l$  is the thickness of the material and  $V$  is the Verdet constant whose value depends on the material itself and in general, the wavelength of incident light.

## 2.2 Malus Law

An empirical approach to analyzing polarization changes is provided by the law of Malus. When the orientation of a linearly polarized light has an angle,  $\theta$ , with respect to the axis of a

polarizer as shown in Figure 1, part of the light will be absorbed when going through the polarizer and the result intensity  $I$  is given by the following equation (2.2.1):

$$I = I_0 \cos^2(\theta) \quad (2.2.1)$$

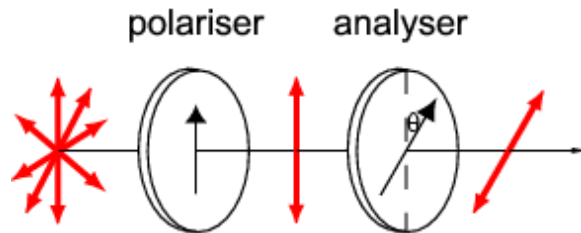


Figure 1. Light Traveling through Polarizers

where  $I_0$  is the intensity of the incident light. Consider the intensity change,  $\Delta I = I - I_0$ , and substitute  $\Delta I + I_0$  for  $I$ . Equation (2.2.1) can be written as:

$$I_0 + \Delta I = I_0 \cos^2(\theta) \quad (2.2.2)$$

Then

$$\Delta I = I_0(\cos^2(\theta) - 1) \quad (2.2.3)$$

In the setup described in Chapter 3,  $\theta$  is the angle between polarizer and analyzer which is 45 degree plus the rotation angle,  $\theta = \frac{\pi}{4} + \theta_F$ . The intensity of the incident light is twice the reference intensity,  $I_0 = 2I_{ref}$ , because  $I_{ref} = I_0 \cos^2(\pi/4) = (1/2)I_0$ . Therefore, equation (2.2.3) can be written as following form:

$$\frac{\Delta I}{I_{ref}} = 2\cos^2\left(\frac{\pi}{4} + \theta_F\right) - 1 \quad (2.2.4)$$

### 2.3 Coherence of Light

It has been well established in classical electrodynamics that light can be treated as transverse electromagnetic wave. The strength of electric or magnetic field of a wave is varying along space and time, as they are determined not only by the amplitude of a wave but also its phase. A simple single-frequency electric wave traveling along an x-axis can be described in mathematical form as following:

$$\vec{E}(x, t) = \vec{E}_0 \cos(kx - \omega t) \quad (2.3.1)$$

where  $\vec{E}_0$  is the amplitude;  $k$  is the wavenumber which is associated with the wavelength of the wave;  $\omega$  is the angular frequency and  $t$  is time. The term  $(kx - \omega t)$  inside the cosine function is called the phase which modulates the strength of the field along space and time. The wave nature of light makes the superposition of multiple light waves affected by both their amplitudes and phases of the combining light waves. Consider the electric field of two waves at the same location to be the following:

$$E_1 = E_{10} \cos(\varphi_1) \quad (2.3.2)$$

$$E_2 = E_{20} \cos(\varphi_2) \quad (2.3.3)$$

where  $\varphi_1$  and  $\varphi_2$  are the phases of two waves. Assuming the fields are in the same direction, they are written in scalar form. The superposition of two waves would be:

$$E_1 + E_2 = E_{10} \cos(\varphi_1) + E_{20} \cos(\varphi_2) \quad (2.3.4)$$

The intensity of the resulting superposition will be proportional to the following:

$$I \propto |E_1 + E_2|^2 = |E_{10} \cos(\varphi_1) + E_{20} \cos(\varphi_2)|^2 \quad (2.3.5)$$

$$= E_{10}^2 \cos^2(\varphi_1) + E_{20}^2 \cos^2(\varphi_2) + 2E_{10}E_{20} \cos(\varphi_1) \cos(\varphi_2) \quad (2.3.6)$$

$$= E_{10}^2 \cos^2(\varphi_1) + E_{20}^2 \cos^2(\varphi_2) + E_{10}E_{20} [\cos(\varphi_1 - \varphi_2) + \underbrace{\cos(\varphi_1 + \varphi_2)}_{\text{time average}=0}] \quad (2.3.7)$$

If  $\varphi_1$  and  $\varphi_2$  have the same frequency, the only term that is independent of time from the expression above would be  $\cos(\varphi_1 - \varphi_2)$  since their frequency components,  $\omega t$ , are canceled out. Since the frequency of light is in order of  $10^{14}$  Hz which is much higher than the speed of most detectors, the intensity we normally observe is its time average. The time average of cosine function and cosine square function are listed below:

$$\langle \cos^2(\varphi_{1,2}) \rangle = \frac{1}{2} \quad (2.3.8)$$

$$\langle \cos(\varphi_1 + \varphi_2) \rangle = 0 \quad (2.3.9)$$

Then the time average of expression (2.3.7) can be calculated as following:

$$\langle (2.3.7) \rangle = \frac{1}{2} E_{10}^2 + \frac{1}{2} E_{20}^2 + E_{10}E_{20} \cos(\varphi_1 - \varphi_2) \quad (2.3.10)$$

To simplify the problem, we ignore some of the constants and write the intensity of the individual wave simply as (2.3.10).

$$I_{1,2} = \frac{1}{2} E_{10,20}^2 \quad (2.3.11)$$

Then the observed intensity of the superposition of two waves will become

$$I = \langle (2.3.7) \rangle = I_1 + I_2 + \underbrace{2\sqrt{I_1 I_2} \cos(\Delta\varphi)}_{\text{interference term}} \quad (2.3.12)$$

where  $\Delta\varphi$  is the phase difference,  $\varphi_1 - \varphi_2$ . It can be seen that the intensity of the superposition is not necessarily the simple addition of their individual intensities. The deviation from the simple

addition case caused by the additional term  $2\sqrt{I_1 I_2} \cos(\Delta\varphi)$  is called interference, an important phenomenon induced by waves. However, it should be noted that we are still assuming the two waves have the same frequency. If their frequencies are much different from each other, resulting in a time dependent phase difference, we must also average the  $\cos(\Delta\varphi)$  term, which then gives us a zero contribution on average from the interference term. In this case, we call those two waves incoherent to each other. The word “coherent” describes the ability of light waves to create interference. Moreover, these two extremes (coherent and incoherent) are not the only two cases of interest. One can also encounter light that can be coherent to some extent. For example, if the frequencies of two waves discussed above are different but very close to each other, causing the phase difference,  $\Delta\varphi$ , only to vary slowly along time, we cannot simply average the interference term because the frequency of the total intensity is slow enough to be observed. In this case the light is called partially coherent. The extent of coherence can be quantitatively characterized by measuring the ability of participating light waves to create interference fringes (a measurable phenomenon directly caused by interference) and it is normally affected by two factors: the monochromaticity and the size of the light source. A detailed discussion of the associated temporal and spatial coherence can be found in books by Gåsvik<sup>[6]</sup> and Pedrotti<sup>[7]</sup>.

In this project, both coherent light and incoherent light is used for illumination. In an early and eventually abandoned design, both coherent and incoherent light caused certain problems which will be discussed in later chapters.

## 2.4 The Huygens-Fresnel Principle and Collimated Light

The Huygens-Fresnel principle is a mathematical framework to describe optical wave propagation and diffraction. The original idea is proposed by Christiaan Huygens that every point on the wave front of optical disturbance serves as a secondary wave source and the amplitude of any point of interest should be the summation of contributions from each secondary source. After development, the principle can be illustrated as following mathematical form:

$$U(P_1) = \frac{1}{i\lambda} \iint_{\Sigma} U(P_0) \frac{e^{ikr_{01}}}{r_{01}} \cos\theta dS \quad (2.4.1)$$

where  $U$  is the amplitude of a given point;  $\lambda$  is wavelength;  $k$  is the wavenumber;  $r_{01}$  is the distance between point  $P_1$  and  $P_0$  and  $\theta$  is the angle between wave propagation direction (the normal direction of the wave front) and the direction of  $r_{01}$  as shown in Figure 2. Equation (2.4.1) illustrates that the amplitude of a point of interest,  $P_1$ , is contributed by all secondary sources,  $P_0$ , on an aperture,  $\Sigma$ .

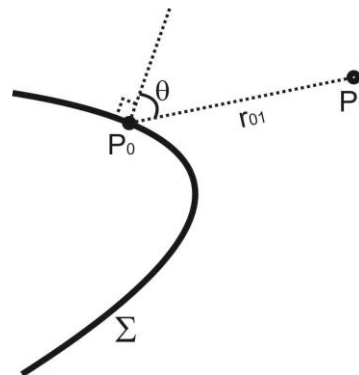


*Figure 2. Illustration for Huygens-Fresnel Principle*



There are several points which should be noted:

(1). All the fields of the wave are assumed to be in the same direction since only scalar values are used in expression (2.4.1) despite its vectorial nature. In this project of magnetic microscope, this assumption is valid since all incident light is linearly polarized.

(2). The amplitude discussed here is complex. This is only for mathematical convenience as the complex number can combine both amplitude and phase together. Only the real part of the complex number contains real physical meaning.

(3). After the establishment of the theory, more advanced theories[8] have shown that Huygens-Fresnel principle can give the right answer for diffraction but the “secondary sources” are not real physical sources but only for calculation purpose.

For a coherent and perfectly collimated light, the light forms plane waves. As the wave propagation is governed by Huygens-Fresnel principle, it can be easily seen that the only way to form a new plane wave is to have an original borderless plane wave, because only in this case the integral is symmetrical for all points on the new plane, thus forming a new plane wave front.

Consider the propagation of a perfect plane wave as described as following:

$$U_{P_1} = \frac{1}{i\lambda} \iint_{-\infty}^{+\infty} U_{P_0} \frac{e^{ikr_{01}}}{r_{01}} \cos\theta ds = U_{P_0} e^{i\varphi} \quad (2.4.2)$$

where  $e^{i\varphi}$  is the phase factor that results from the wave propagation. Then, a small disturbance at point  $P'_0$  of the wave front,  $\Delta U$ , is introduced, so the integral for the next plane becomes:

$$U'_{P_1} = \frac{1}{i\lambda} \iint_{-\infty}^{+\infty} [U_{P_0} + \Delta U \delta(P'_0)] \frac{e^{ikr_{01}}}{r_{01}} \cos\theta ds \quad (2.4.3)$$

$$= \frac{1}{i\lambda} \iint_{-\infty}^{+\infty} U_{P_0} \frac{e^{ikr_{01}}}{r_{01}} \cos\theta ds + \frac{1}{i\lambda} \iint_{-\infty}^{+\infty} \Delta U \delta(P'_0) \frac{e^{ikr_{01}}}{r_{01}} \cos\theta ds \quad (2.4.4)$$

$$= U_{P_0} e^{i\varphi} + \frac{1}{i\lambda} \iint_{-\infty}^{+\infty} \Delta U \delta(P'_0) \frac{e^{ikr_{01}}}{r_{01}} \cos\theta ds \quad (2.4.5)$$

$$= U_{P_1} + \underbrace{\frac{1}{i\lambda} \Delta U \frac{e^{ikr_{01}(P'_0)}}{r_{01}(P'_0)} \cos[\theta(P'_0)]}_{\text{spherical wave term modulated by } \cos\theta} \quad (2.4.6)$$

It means the result of the disturbance at a single point is to create a spherical wave term in the future propagation as shown in equation (2.4.6). The disturbance will damage the collimation since the spherical wave propagates in a wide angle although it is modulated by the angle term,  $\cos\theta$ .

In a preliminary design of the imaging system, it is assumed that a collimated light can still be well collimated after it passes a sample with spatial transmittance variance. However, as discussed above it is theoretically impossible. The preliminary design is abandoned mainly due to this theoretical complication.

## 2.5 The Fourier Transform Introduction

### (1). One-dimensional Fourier transform

The existence of the Fourier transform is based on the fact that any function could be represented by a series of base functions (a basis set) when some mathematical conditions are met. Those mathematical conditions could be defined in different ways and be equally sufficient. The conditions concern both base functions and the function being represented. A common set of these conditions include that the function being represented should be absolutely integrable over the domain of definition and have only a finite number of discontinuities and a finite number of maxima and minima in any finite range<sup>[8]</sup>. Base functions should be orthogonal to each other and complete. However, the strict mathematical concept is not the focus of our discussion because signals in real physical world mostly meet all mathematical requirements or the error caused by the deviation is negligible.

In one-dimension, the base functions can be the complex exponential functions, which is illustrated as following:

$$g(t) = \int_{-\infty}^{+\infty} G(\omega)e^{i\omega t} d\omega \quad (2.5.1)$$

This means any function  $g(t)$  could be represented by the combination (integral) of a family of complex exponential functions,  $e^{-i\omega t}$ , where  $\omega$  is usually called frequency. The coefficient function,  $G(\omega)$ , is called the Fourier transform of  $g(t)$  since  $G(\omega)$  determines the amplitude of each base function, thus representing  $g(t)$  in terms of  $e^{-i\omega t}$ .

Equation (2.5.1) also presents the way to calculate  $g(t)$  when  $G(\omega)$  is known. This process is called inverse Fourier transformation:

$$g(t) = \int_{-\infty}^{+\infty} G(\omega)e^{i\omega t} d\omega = \mathcal{F}^{-1}\{G(\omega)\} \quad (2.5.2)$$

Furthermore, there exists the Fourier transformation:

$$G(\omega) = \int_{-\infty}^{+\infty} g(t)e^{-i\omega t} dt = \mathcal{F}\{g(t)\} \quad (2.5.3)$$

It is important to note that complex exponential function  $e^{-i\omega t}$  is associated with sine and cosine function:

$$e^{i\omega t} = \cos(\omega t) + i \cdot \sin(\omega t) \quad (2.5.4)$$

which is the reason why this expansion is of great importance in many fields of science and engineering. Many physical signals consist of sinusoidal components such as light and alternating current. In addition, the frequency,  $\omega$ , usually has important physical meaning which indicates how the signal repeats itself spatially or temporally. For example, if  $g(t)$  means a signal varying along time,  $t$ , and has a peak frequency, then the peak frequency here,  $\omega_{peak}$ , means the signal will generally repeat itself every  $2\pi/\omega_{peak}$  time. Note that in the integral there are components associated with negative frequencies which does not have real physical meaning. However, if one only takes the real part of the complex exponential function into consideration, it is obvious that the negative frequency has same physical meaning as its positive counterpart.

## (2). Two-dimensional Fourier transform

The two-dimensional Fourier transform is the generalization of the one-dimensional case, which is illustrated as following:

$$g(x, y) = \mathcal{F}^{-1}\{G(f_x, f_y)\} = \int_{-\infty}^{+\infty} \int_{-\infty}^{+\infty} G(f_x, f_y) e^{i2\pi(f_x x + f_y y)} df_x df_y \quad (2.5.5)$$

$$G(f_x, f_y) = \mathcal{F}\{g(f_x, f_y)\} = \int_{-\infty}^{+\infty} \int_{-\infty}^{+\infty} g(x, y) e^{-i2\pi(f_x x + f_y y)} dx dy \quad (2.5.6)$$

Similar to that the function is determined by two variables  $(x, y)$ , the Fourier transform is also determined by two frequencies  $(f_x, f_y)$ . If  $g(x, y)$  is treated as a two-dimensional signal

distribution, such as a greyscale image, the frequencies  $(f_x, f_y)$  here represent how signal repeats itself across the image. For example, the image of vertical fringes shown in Figure 3 only contains a single-frequency component along the horizontal direction. In Figure 3, the white stripe tends to repeat every after a certain distance along the horizontal direction, which corresponds to certain frequency  $f_x$ .

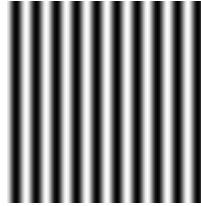


*Figure 3. Fingle-Frequency Component*

Unlike real-life scenarios of the one-dimensional case where frequency is usually associated with time, the frequencies here are more often connected to the signal distribution over a two-dimensional map, a space related parameter, so in the two-dimensional case these frequencies are usually called spatial frequencies. More detail can be found in the book by Goodman<sup>[8]</sup>.

### (3). Discrete Fourier transform (DFT)

Discrete Fourier transform converts a sequence of discrete data into another equal-length sequence of data, which is defined as following:

$$y_{p+1} = \sum_{j=0}^{n-1} x_{j+1} e^{-\frac{i2\pi jp}{n}} \quad (2.5.7)$$

where  $n$  is the length of the sequence and  $p = 0, 1, 2 \dots n - 1$ . This transform has a mathematic structure similar to the Fourier transform illustrated before. Moreover, it can be demonstrated that  $y_p$  generally is a representation of  $x_j$  in frequency domain. In more detail, if  $x_j$  is an equal-spacing

sampling of a continuous function  $x(t)$  and some prerequisites are satisfied: (1) the continuous function  $x(t)$  is band-limited; (2) the sampling rate is no less than twice the maximum frequency limit of  $x(t)$ ,  $y_p$  then is an equal-spacing sampling of the Fourier transform of  $x(t)$ <sup>[9]</sup>. Although for a finite number of data in a limited range (assuming zero value for anywhere out of the range), theoretically it could not be band-limited in frequency domain, thus introducing an error, we assume this error is negligible in our analysis.

DFT is a more practical way of doing Fourier transform in science and engineering since most of our detectors only offer a discrete sampling of a continuous signal. As for the two-dimensional case, the two-dimensional DFT is also a simple generalization of one-dimensional DFT as discussed in (2).

In this project, Fourier analysis is used to eliminate noise with certain frequencies and to analyze the frequency distribution of the images acquired by the system.

### 3. SETUP CONCEPT INTRODUCTION

In this section, basic setup elements and the general concept are described.

The basic schematic of the setup is illustrated in Figure 4. To induce certain magnetic response including Faraday rotation, an external magnetic field in pulse form is applied to the sample. The field is generated by a solenoid connected to a capacitor bank. The peak value of the pulse is around 0.5T depending on the voltage applied and the duration of the pulse is around 200ms (also dependent on the applied voltage). More detailed information about the pulse field generator is given in the paper by Thomas Foulkes<sup>[10]</sup>.

The sample to be investigated is placed at the center of the solenoid, where it is to be subjected to a spatially uniform magnetic field pulse. Collimated and linearly polarized light is deployed incident upon the sample inside the solenoid, where the polarization state of the incident light may change when the pulse magnetic field is applied. After that, another polarizer 45 degrees with respect to the first one is placed after the sample, serving as an analyzer. The light signal after the analyzer then is collected by a photodetector and/or a camera to perform imaging and/or intensity detection. If the polarization state has not changed, a reference level of signal can be detected which should be half the intensity before the analyzer according to Malus's law. When the polarization is rotated towards or away from the axis of the analyzer, a signal increase or decrease is expected. The angle of the polarizers is 45 degree because in this case the clockwise and anti-clockwise rotation can be distinguished and the intensity change is almost linear to the rotation angle. The difference between the received signal level and the reference level can be used to

measure the polarization change such as rotation angle or the ellipticity change of the signal light. If the sample is inhomogeneous regarding its magnetic property, the polarization change is expected to be different over the illuminated area, thus creating an image after passing through the analyzer.

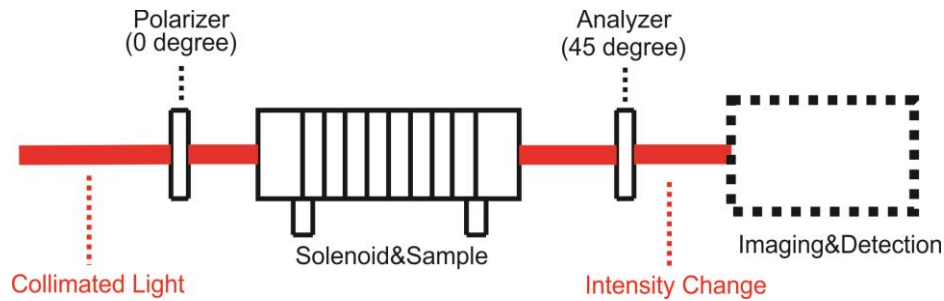


*Figure 4. Basic Setup Schematic*

For example, imagine that a 3x3 image is acquired before the pulse field is applied which has a reference level of  $I$ , as shown below in Figure 5.

$I$	$I$	$I$
$I$	$I$	$I$
$I$	$I$	$I$

*Figure 5. 3 by 3 Image*

After the field is applied, due to a difference in magnetic properties in each pixel, each pixel would experience an intensity change shown in Figure 6.



$I+\Delta I_1$	$I+\Delta I_2$	$I+\Delta I_3$
$I+\Delta I_4$	$I+\Delta I_5$	$I+\Delta I_6$
$I+\Delta I_7$	$I+\Delta I_8$	$I+\Delta I_9$

*Figure 6. Intensity Change in Each Pixel after Pulse Is Fired*

The relative intensity change is calculated by comparing the intensity level before and after the field is applied as shown in Figure 7. This relative intensity change is directly associated with the change of the polarization state of light.

$\frac{\Delta I_1}{I}$	$\frac{\Delta I_2}{I}$	$\frac{\Delta I_3}{I}$
$\frac{\Delta I_4}{I}$	$\frac{\Delta I_5}{I}$	$\frac{\Delta I_6}{I}$
$\frac{\Delta I_7}{I}$	$\frac{\Delta I_8}{I}$	$\frac{\Delta I_9}{I}$

*Figure 7. Image of Relative Change*

Theoretically, if the beam is perfectly collimated through the sample and the intensity change is caused only by Faraday rotation, the relative intensity change is linked with the Verdet constant of the material by the following equations:

$$\frac{\Delta I}{I} = 2\cos^2\left(\frac{\pi}{4} + \theta_F\right) - 1 \quad (3.1.1)$$

$$\theta_F = BV \quad (3.1.2)$$

where  $\theta_F$  is the Faraday rotation angle;  $B$  is the amplitude of the magnetic field in the direction of the light propagation;  $l$  is the thickness of the sample and  $V$  is the Verdet constant. The introduction about the Faraday rotation and the deduction of the first equation can be found in the Chapter 2.

## 4. PRELIMINARY SETUP DISCUSSION

A preliminary setup design is discussed in this chapter. The design was eventually changed due to theoretical misunderstanding and its high sensitivity to collimation, but the encountered problems are still discussed in this chapter, as they helped refine the design for the final setup.

### 4.1 Preliminary Setup Description

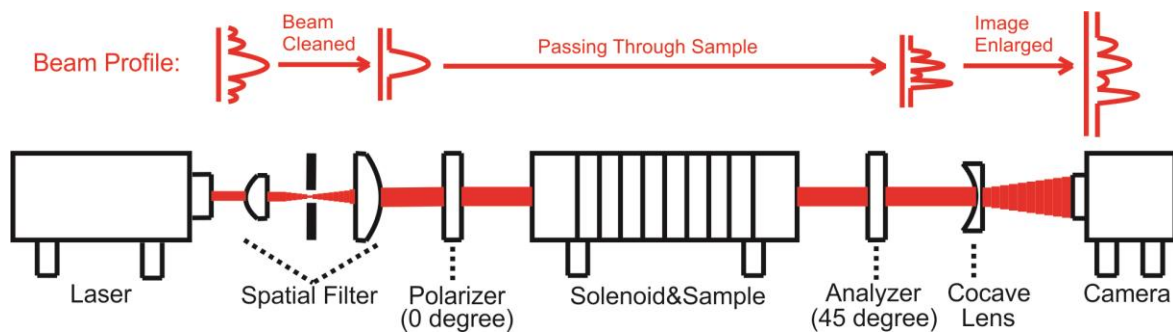


*Figure 8. Schematic of the Preliminary Setup*

The preliminary setup for laser source is described in Figure 8. The spatial filter is used to clean the beam profile to provide a more even intensity distribution. In early stages, it was assumed that the light is still collimated even after the image is formed because there is no lens or other optical components that could cause light to converge or diverge between the polarizer and analyzer. Basically, it was assumed that the light after the analyzer is still collimated except having a non-uniform intensity profile. However, this assumption is theoretically wrong and it is explained in detail in Section 2.4. Assuming the image is already formed without using any traditional

imaging system, the one problem left is how the image can be magnified for higher resolution at the detection end. At first, a simple concave lens ( $\text{Ø}6\text{mm}$ ,  $f=-6\text{mm}$ , N-SF11 plano-concave lens) was used to diverge the beam in order to create an enlarged image as shown in the Figure 8 above. The magnification could be continuously adjusted by adjusting the distance between the concave lens and the camera. The flexibility and simplicity were seen as major attractive features of this design.

Both coherent laser light (He-Ne laser) and incoherent white light are used in the setup as the schematic of white light setup is shown in the Figure 9. To avoid any chromatic aberration, white light is collimated using an optical fiber (core size 400 $\mu\text{m}$ ) and a parabolic mirror. The exiting port of the fiber serves as a point source and is placed at the focal point of the parabolic mirror. Choosing core size of the fiber is a compromise between collimation quality and light throughput. Smaller core size of the fiber will improve the quality of the collimation but also reduce the light throughput. Detailed information about components used in the preliminary setup can be found in the Appendix 2.

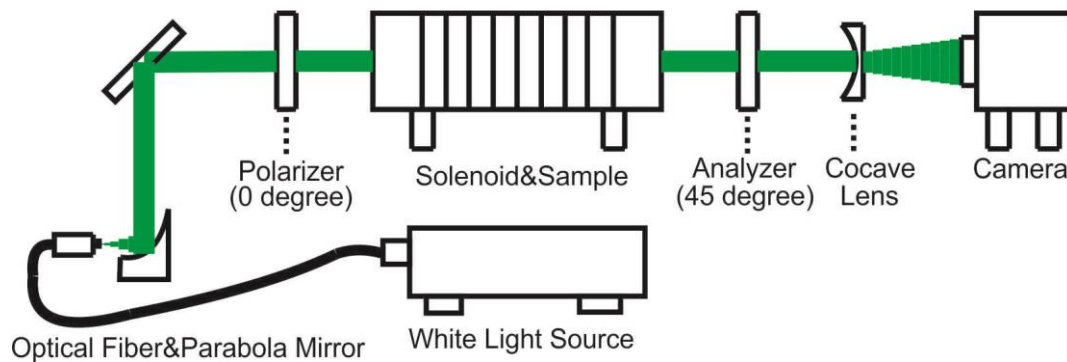


*Figure 9. The Preliminary Setup for White Light*

## 4.2 Problems Encountered in the Preliminary Setup

During construction and testing of the setup, problems regarding both laser and white light source emerged and eventually the design was completely changed. However, as part of the process, some of the problems are still worth discussing and they will be generally described and analyzed in this section.

The main problem of the laser based setup originates from its coherent nature. As the laser light passes through different optical components (polarizer, lens and sample), diffraction induced by those components creates unwanted diffraction patterns that can negatively affect the resulting images. For this application, the only important information is the relative change of the signal level, which in theory makes the uneven reference level irrelevant because for a different local reference level the change will be different accordingly, making the final relative change the same value. However, in practice, an unevenly distributed intensity profile can affect the resulting image negatively for two reasons.

The first one is that lower the reference level could result in a lower signal to noise ratio in that area. Normally a diffraction pattern is a shape consisting of dark and bright fringes. In the dark area of the fringes the signal will be affected more by the noise level of the camera. With the presence of the noise, the intensity of the pixel is constantly changing randomly in a limited range even without any field applied, so there is always a noise related intensity change,  $\Delta I_{noise}$ , no matter what two images are compared to each other. Therefore, if  $\Delta I_{noise}$  is included, the operation for every pixel becomes:

$$relative\ intensity\ change = \frac{\Delta I + \Delta I_{noise}}{I} \quad (3.3.1)$$

Though  $\Delta I_{noise}$  is associated with both electronic circuit noise and the signal level,  $\Delta I_{noise}$  generally starts to become significant if the polarization related intensity change,  $\Delta I$ , and the reference level,  $I$ , are low. In practice,  $\Delta I_{noise}$  becomes a problem when strong diffraction pattern which includes dark fringes is present and when samples with weak response are measured. For instance, nickel films are measured during the testing of the microscope. Though nickel is a strong ferromagnetic material, with thickness of 50-100nm, the transmittance is very low (below 0.4%). Following are a raw image of a uniform 50nm thick nickel film (Figure 10) and the processed image (Figure 11) after calculating the relative intensity change.

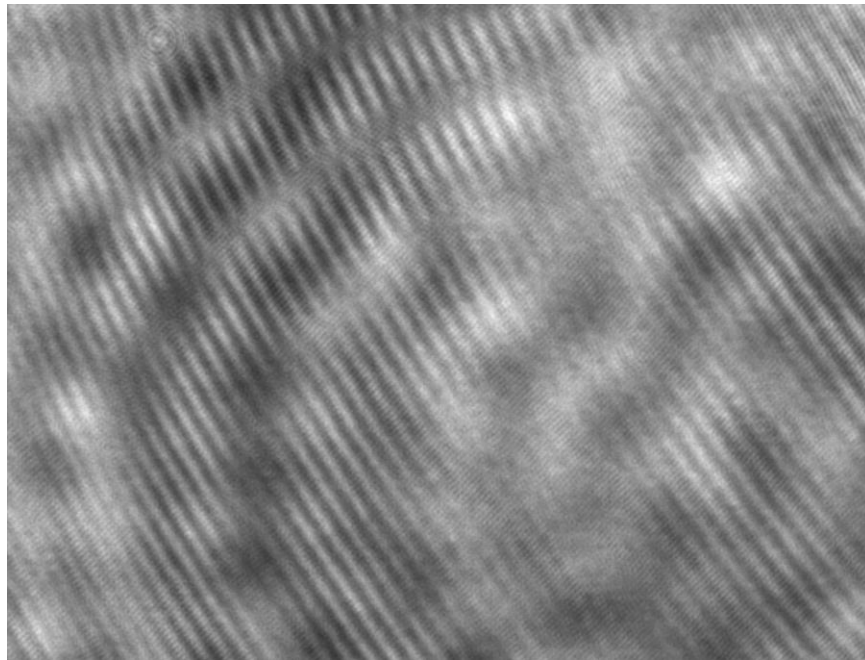


*Figure 10. Raw Image of a Uniform Nickel Film under Laser Setup*

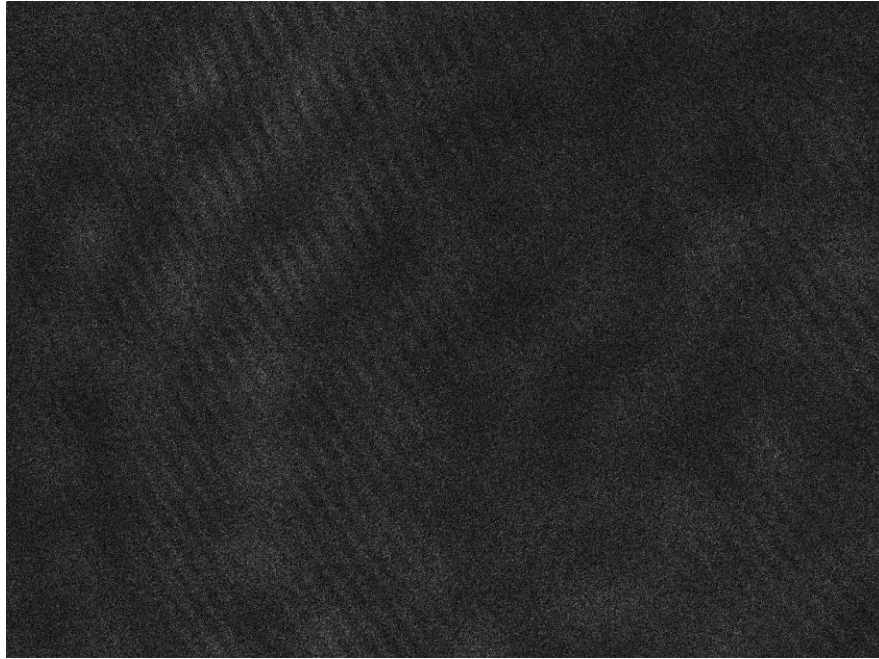


*Figure 11. Processed Image of the Measurement*

As shown in the raw image, multiple layers of diffraction patterns are present, creating bright and dark areas. With the intensity change,  $\Delta I$ , very small, the processed image resembles the diffraction pattern of the raw image. The image is brighter where the dark fringes are in the raw image. It is because since the level of  $\Delta I_{noise}$  almost constant over the image, the relative change is mostly determined by the denominator of the operation, the reference level.

To resolve this problem, the unwanted diffraction pattern and any other things that could produce high contrast in the raw image should be reduced as much as possible. At the same time, signal to noise ratio should be increased so that the noise would not have a big impact on the result image. Normal ways of increasing signal to noise ratio include accumulating signal by increasing integration time or averaging multiple measurements. Since the magnetic field produced by the capacitor bank is in pulse form, signal cannot be accumulated over time. Labview programs have been developed to integrate hardware to perform multiple measurements automatically for

averaging. Assuming the response of the sample does not change, results from multiple measurements can be added together and averaged to improve the signal to noise ratio. This assumption is not necessarily valid for highly ferromagnetic samples. Details about the programs are described in Appendix 3.

The second way that low signal intensity may negatively affect the result image is that it may lower the accuracy of the measurement due to limited pixel depth (or dynamic range) of the camera. For example, the camera used in the preliminary design only has 8-bit pixel depth (Thorlabs DCU223C) so the dark fringes usually have digital output of 30-40 (in the range of 0-256) without saturating the brighter area. This means the minimum sensitivity for intensity change is no higher than about 3%. A new camera with 16-bit pixel depth is used to improve this accuracy.

As seen in Figure 10, there are multiple layers of diffraction patterns created by different components of the system. The ring-shaped pattern (shown in Figure 12(c)) near the top-left corner of Figure 10 is created by a dust particle on the camera protective glass; the big wavy pattern (Figure 12(a)) is created by blocking some of the laser beam with an iris; the backslash-shaped lines (Figure 12(d)) are formed because of the interference caused by the camera protective glass and the very small features (Figure 12(b)) are related to the aperture size of the concave lens. These sources of diffraction are found by observing the change of the fringes when moving or changing one of the components.



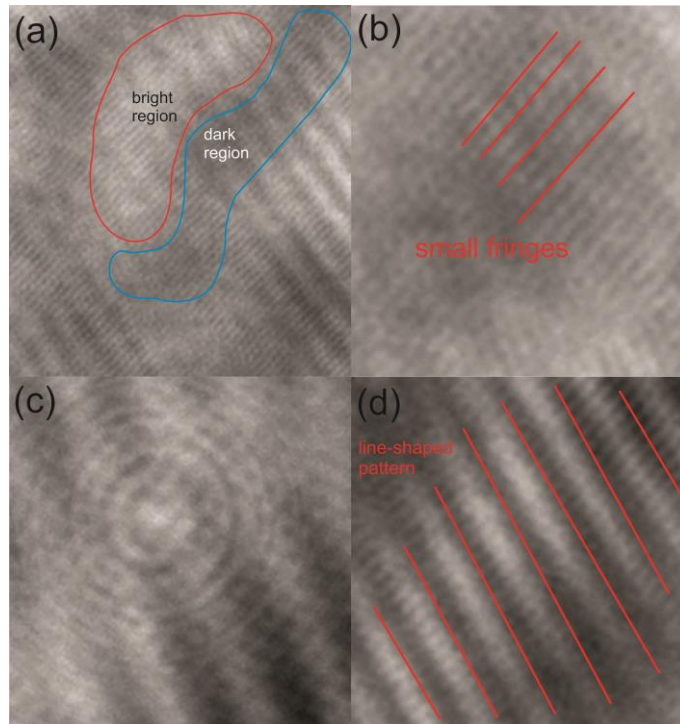


Figure 12. (a) Big wavy fringes; (b) Small structures; (c) Ring-shaped diffraction pattern and (d) Backslash-shaped lines.

Moreover, the diffraction patterns created by the sample itself is a bigger problem than that created by other components because it is directly linked with final imaging. One mistake made in early stages of the project is to assume that coherent light can be perfectly collimated despite an unevenly distributed intensity profile. However, according to Huygens-Fresnel principle (explained in Section 2.3), there does not exist a collimated plane wave with a non-uniform amplitude distribution. Once the amplitude at one point is changed to be different from other points, the symmetry is broken and the interference of the secondary wave sources will not form plane wave anymore. Instead, the wave front will be distorted and contains light components propagating in other directions and forming diffraction patterns. This problem makes it almost impossible to achieve quality images in this early setup with coherent light. The signal can be detected without diffraction in the near-field region ( $\sim \lambda$ )<sup>[11]</sup> but this option is not practical for this project. After

changing the design into a conventional microscope setup, the diffraction problem from the sample is partially resolved, which is detailly discussed in chapter 4.

Incoherent white light with a wide bandwidth is also used in the setup. Since diffraction is not a primary concern for incoherent light, the diffraction problems discussed above are naturally solved by changing into incoherent light source. However, there are other issues emerging with the incoherent light. To collimate the incoherent light, the size of the source should be as small as possible. However, using a small size light source to create collimation is at expense of overall light throughput. After testing, it has been found that the preliminary design is very sensitive to the quality of collimation and the current hardware available to us is not enough to create a quality image. This problem can also be solved with a conventional microscope since collimated light is not required to form an image for conventional microscope.

## 5. FINAL SETUP INTRODUCTION

In this chapter, the final setup is introduced and described in detail. Additional discussion of problems encountered during the design phase, and their solutions are also presented. A schematic of the final setup is shown in Figure 13.

### 5.1 Final Setup Description

In the final setup, a conventional microscope is built upon the solenoid which is connected to the pulse magnetic field generator. The microscope basically consists of 10X objective (Mitutoyo MY10X-803) and a tube lens (currently a simple spherical lens,  $f=200\text{mm}$ ). Because the objective is infinity corrected, light from one object point will be collimated between the objective and tube lens (the direction of the collimated beam is determined by the location of the object point). Therefore, the polarizer and beamsplitter are placed in this region because the angle of the incident light is smaller for the polarizer and no additional spherical aberration is added into the system. Multiple light sources and detectors are coupled with the system as shown in the Figure 13. This is done to minimize the time that would be spent aligning the system every time a light source is switched. The spatial filter is used to clean the beam and provide a more evenly distributed intensity profile. Detailed information about optical, mechanical and software components are described in Appendix 1, 3, 4. After some testing of the system, some problems with laser wide-field imaging remain as discussed in the following section. Thus, currently only white light is used

for imaging testing. In this setup, the laser is instead used for intensity measurement and system alignment.

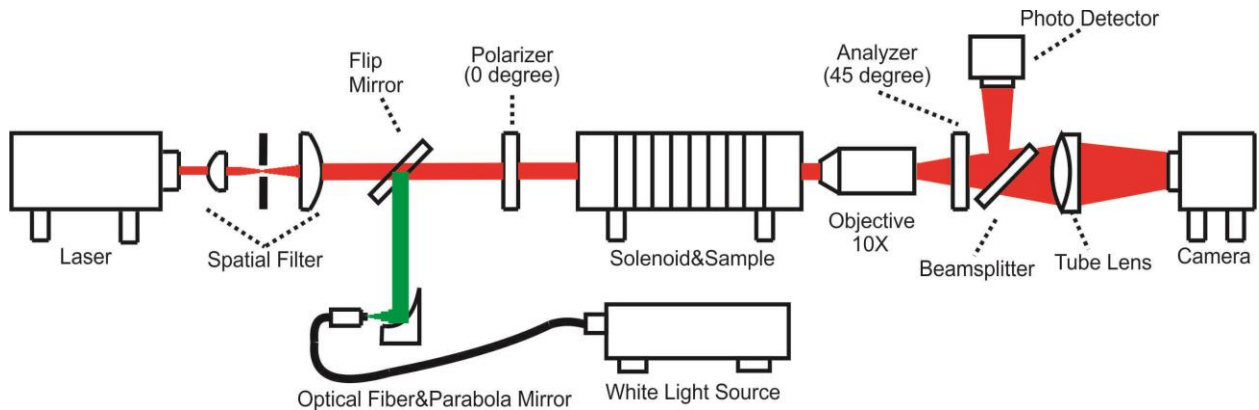


*Figure 13. Schematic for Final Setup*

## 5.2 Problems of Laser Wide-Field Imaging

In a conventional microscope, all light from an object point is collected and imaged to corresponding image point, which ideally will not produce any diffraction pattern even with a laser source. This conclusion can be examined using Huygens-Fresnel principle as shown in Figure 14. Consider all secondary wave sources on the object plane. In theory, the wave from each source is collected by the imaging system and then converged again into point at the image plane. Therefore, there is no interference between secondary sources at the image plane, so no diffraction pattern will be induced by the spatial variation of the sample itself.

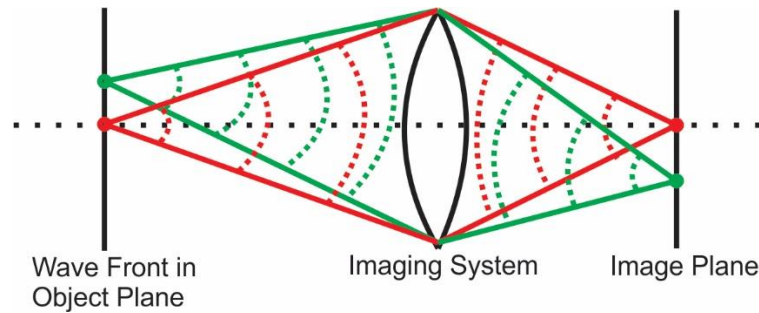


*Figure 14. Optical imaging system*

As discussed in Chapter 4, sample-induced diffraction pattern is a major problem for imaging using coherent light. Though this problem is well managed with conventional microscope setup, the diffraction patterns induced by aberration, iris size and the camera protective glass still remain in the system. While the aberration and iris related diffraction can be reduced by using optical components with low aberration and adjusting the iris size, the diffraction pattern induced by the camera protective glass is very stable and hard to eliminate physically without changing the camera. Since the diffraction pattern related to the protective glass is very stable in terms of direction and frequency, this pattern could be removed by using two-dimensional DFT. It is still difficult to remove all the diffraction patterns, but various methods can be used to suppress them to the point where they will have minimum impact on the final processed image.

Another major problem encountered when using laser light for imaging is the mechanical vibration of the system induced by the magnetic pulse field. While it is indeed a critical problem, the scale of the displacement is on the order of microns during the peak period of the pulse. When operating with high field (high peak value of the pulse), the rapidly changing pulse field will make three parts of the system vibrate: the solenoid, the samples made of magnetic material and the objective. The vibration will cause the field of view to change during measurements. Since the image processing includes comparing two images before and during the pulse (illustrated in

Section 3.1), the movement of the field of view will break the pixel to pixel mapping. Apart from the change of field of view, the remaining interference fringes tend to vibrate more than the image itself since fringes are normally very sensitive to system movement. While vibrations can be minimized by isolating the sample from the solenoid and clamping down the objective housing, the movement of the fringes is still relatively severe, which will make the intensity of a pixel much less accurate to represent local polarization change. An example image is provided below (Figure 15) which is a nickel film imprinted with a random pattern (100 nm thick in dark area, 50 nm thick in bright area). When the pulse is fired, the fringes are vibrating more than the image itself.

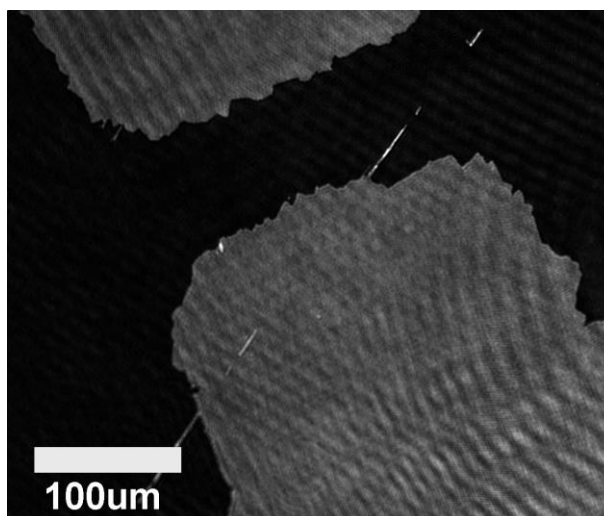


*Figure 15. Example Image Using Laser Wide-Field Imaging*

Currently, laser light is not used for imaging due to severe vibration and diffraction issue despite its superior monochromaticity and collimation. Further suggestion is made that arc lamps such as a mercury or xenon lamp can be used to provide incoherent light with good monochromaticity.

## 6. FINAL SETUP TESTING

In this chapter, several testing results are presented to characterize the system. The parameters of great interest are the resolution and sensitivity of the system. The resolution is tested based on the assumption that although the images are processed after measurements, the inherent optical resolution of the system does not depend on magnetic field. Therefore, the resolution of the system is tested without applying the field using a normal resolution target. The sensitivity of the system is tested in terms of relative intensity change: how much relative intensity change is needed to provide enough contrast in a processed image. It should be noted that the sensitivity is closely associated with the signal to noise ratio and could be improved by using the automatic measurement program in LabVIEW described in Appendix 3. In this chapter, sensitivity is measured with certain experimental parameters.

### 6.1 Magnetic Field Calibration

The relation between the peak value of the pulse magnetic field and the voltage applied is measured using a Gauss probe (FW Bell 5180). The Gauss probe is inserted in the middle of the solenoid where the field is considered uniformly distributed. The relation is almost linear and is given in Figure 16.

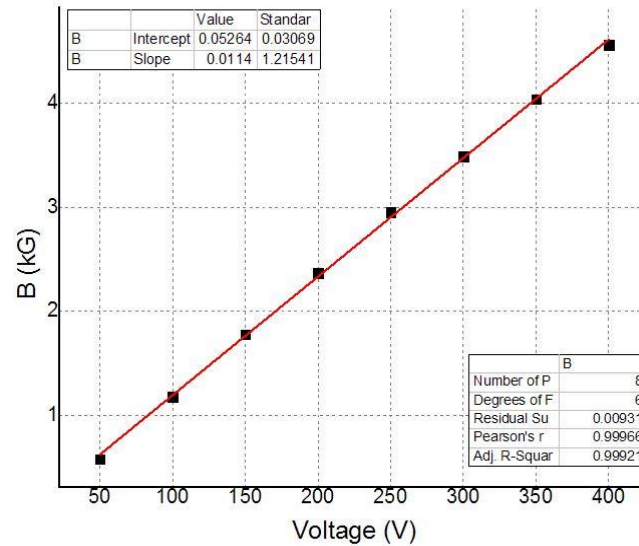


Figure 16. Relation between Peak Field Value and Voltage (a line is fitted to the data)

## 6.2 Water Measurement for System Testing

A measurement for water is done using He-Ne laser (633nm) at a capacitor charging voltage of 100V. Only a photodetector (shown in Figure 13) is used in this measurement so no imaging is involved. This test is to verify the field calibration and test the system working state by calculating the Verdet constant of water. The raw data of the measurement is shown in Figure 17 (the explanation of the data is in the caption). It can be noticed that there is a frequency component in the light intensity signal (the blue curve). The component is due to electronic noise with a very stable frequency of 60Hz. This noise can be reduced digitally using DFT algorithm (explained in Section 2.4) and the processed data is also shown in Figure 17.

From the current signal data (peak signal: 0.251V in Figure 17), transfer ratio of the current censor (15mV/A) and the known parameters of the solenoid<sup>[10]</sup> (610 turns in total and 10.7cm long),



the peak field value can be calculated by using the formula of magnetic field generated in a solenoid, as shown in equation (6.2.1).

$$B = \mu_0 \cdot I \cdot n = \mu_0 \cdot \frac{V_I}{\sigma} \cdot \frac{N}{L} = \left( 4\pi \cdot 10^{-7} \cdot \frac{251}{15} \cdot \frac{610}{0.107} \right) T = 0.1198T \quad (6.2.1)$$

where  $\mu_0$  is permeability of vacuum;  $I$  is the current inside the solenoid;  $n$  is the turns per length;  $V_I$  is the signal value of the current sensor;  $\sigma$  is the transfer ratio;  $N$  is the total turn number and  $L$  is the length of the solenoid. The calculated result (1.198kGauss) is consistent with the directly measured result (1.180kGauss) with 2.2% error.

Instead of raw light signal, a processed light signal (green curve in Figure 17) is used to calculate the Verdet constant. Note that water is a diamagnetic material and has a fast response to an external magnetic field. In this case, Verdet constant is calculated for every point during the pulse from maximum to half maximum using equation (2.1.3) and (2.2.4). The reference light intensity,  $I_{ref}$ , in equation (2.2.4) is calculated by averaging all the signal before pulse. The magnetic field,  $B$ , is calculated using equation (6.2.1) with the current data (red curve in Figure 17) After averaging all the Verdet constant results to minimize the effect of noise, a final result of  $1.983 \cdot 10^{-4}$  degree/Gauss·cm is given by the calculation. This result has a 3.3% error compared with the reference value,  $1.919 \cdot 10^{-4}$  degree/Gauss·cm at 633nm. This error can be caused by multiple factors such as the uncertainty of the light intensity signal due to noise level, error introduced by magnetic field calculation and even the purity of the water sample. Therefore, for testing purpose, this error is acceptable.

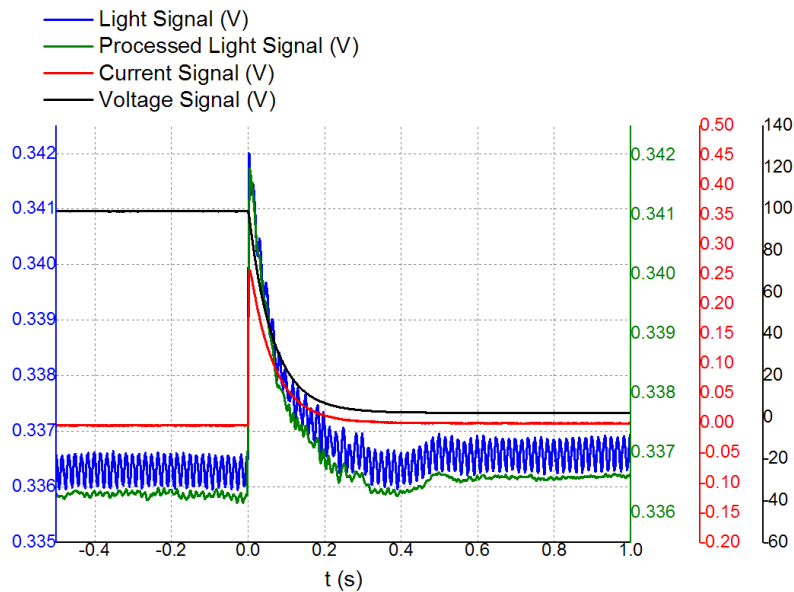
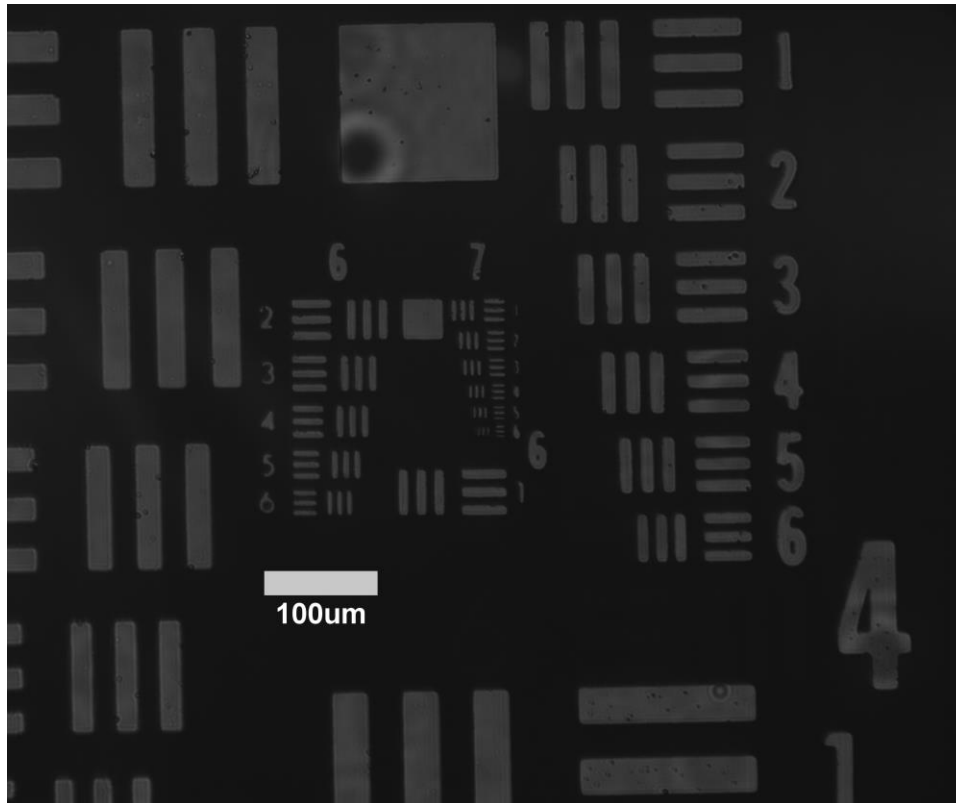


Figure 17. Raw Data of Intensity Measurement at 100V: blue curve is the light intensity after the analyzer which is monitored by the photodetector; green curve is the processed light intensity where the 60Hz noise has been removed digitally; red curve is the current running through the solenoid and the black curve is the voltage applied on the capacitor. All signals are converted into voltages and input to an oscilloscope.

### 6.3 Optical Resolution Test

A resolution test is done to test the resolution of the microscope which is described in Appendix 1, part 11. The model of the resolution target is Newport RES-1 which conforms to the USAF-1951 resolution target standard. The white light is used for illumination. The image captured is shown in the Figure 18. It can be seen that the finest structure of the target (the element 6 in group 7 and its resolution is 228l/mm) can still be resolved.



*Figure 18. Resolution Target Imaging*

This is a simple resolution test so no magnetic field is applied. This is because based on the image processing method, the processed image should not be different from the raw images in terms of resolution. Therefore, the optical resolution of the microscope can be treated as the resolution of the system.

#### 6.4 Sensitivity Test

The sensitivity here is defined as the least intensity change the system can detect. It is tested by using a metal film deposited on a thin glass substrate. The deposition process is described in Appendix 5. Half of the film is made of 50nm thick aluminum and the other half is made of 50nm thick nickel. The aluminum and nickel film have very similar transparency but aluminum has very

weak response to magnetic field while nickel is a strong ferromagnetic material. The purpose of making this film is to create an artificial difference in terms of magnetic response so an image can be achieved. Therefore, whether the system can detect the intensity change can be determined by whether an image can be formed. The transparency is similar for both parts (nickel and aluminum) so that even when the signal is weak, noise level will not have different effects on two parts of the film.

Due to the low transparency of the metal film (transmittance with white light source: 0.4%) and small throughput of the white light illumination (most of the white light is blocked to ensure better collimation), not much signal could be collected. In order to enhance the signal to noise ratio, 50 measurements are made automatically and added together. Each measurement consists of a 2.5 second recording with 65frame/s and a magnetic pulse fired during the recording. Details on the automatic measurements are explained in Appendix 3. There is a one minute time interval between measurements to avoid heat buildup in the solenoid.

Figure 19 is one of the raw images captured during one measurement. The nickel is on the right side and the aluminum is on the left side. The dark area is where aluminum and nickel overlap so it is darker than other areas. The bright spots on the right side are defects of the film.

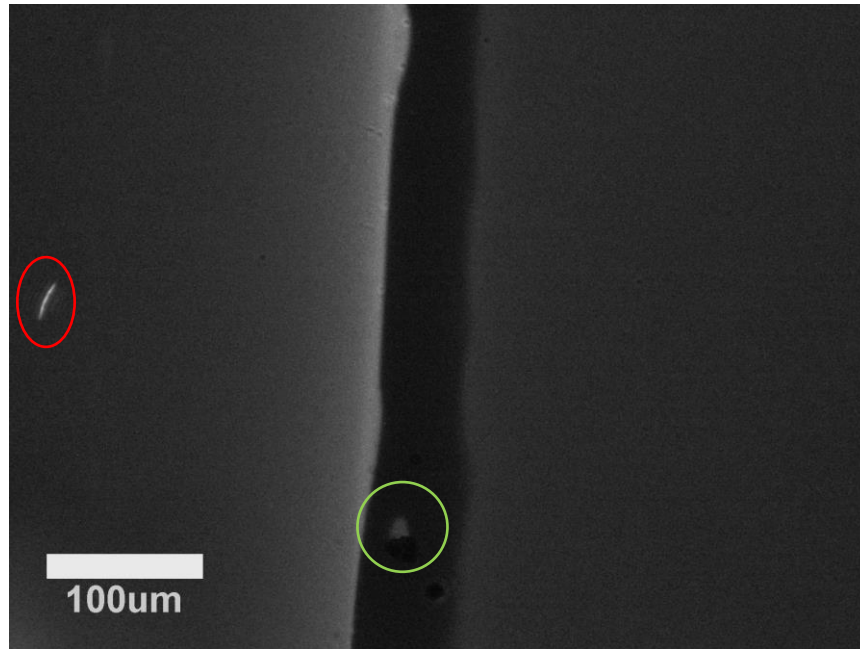


*Figure 19. Aluminum and Nickel Film (aluminum on the left and Nickel on the right)*

The images captured by the system will undergo a process of comparing images before and during the pulse, which is explained in Section 3.1. The image during the pulse is determined by picking the image of maximum change of intensity which happens at the peak of the pulse. The image before the pulse is calculated by averaging 20 images before the pulse to reduce noise level. After processing the images for each measurement, the results of 50 measurements will be added together. Because the relative change is very small, the value of each pixel is then multiplied by another factor to enhance the contrast. In this case, the enhancement factor is 800000. The result image is shown in Figure 20. The relative intensity change of the image is about 1% on average. One can easily tell that the right side of the image is brighter than the left side, which is due to the difference in their magnetic properties. In this case, the system is able to detect 1% intensity change.

Notice that there are some blurry features (circled in red and green) in the image. Those features are caused by the averaging over multiple measurements. As described in section 5.2, the

magnetic pulse field may cause the field of view to change on a small scale (1-2 $\mu$ m) in each measurement. Therefore, the cumulative effect of 50 measurement on the processed image is the blurry features circled in Figure 20.

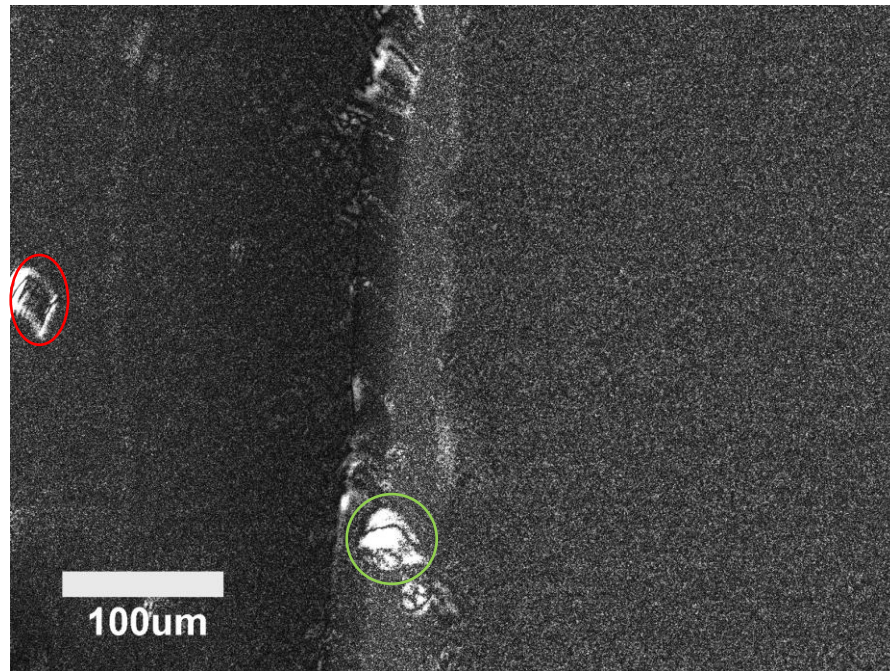


*Figure 20. Processed Image for Sensitivity Testing*

It should be noted that the sensitivity of this system can be affected by multiple factors and is strongly associated with the signal to noise ratio, so the sensitivity is only meaningful when the experimental parameters are specified. The sensitivity tested here is for a case where only weak signal can be detected so it should be close to the limit of the system. However, if signal to noise ratio is high enough for one measurement, no averaging is needed and will not be affected by the movement of field of view.

## 7. FUTURE WORK

In this chapter, possible improvements for the system and samples of interest are discussed.

### 7.1 Imaging of Liquid and Solid Samples

Apart from the system testing, some samples are also investigated using the system. They are briefly discussed in this chapter and are part of ongoing research. One class of systems that we are currently interested in is in suspension form such as suspension of magnetic particles and blood samples. The nanoparticles or blood cells in a liquid environment can have response to magnetic field. Their tendency of forming clutters, aggregates and chains is documented in previous papers<sup>[12-14]</sup>. Efforts are made to observe their behavior under a quickly changing magnetic field. However, because of some instrumental limitations, this behavior has not been clearly observed.

One limitation is that the microscope is designed to image one plane but the cells currently available to contain the suspension are 1-2cm in length, so most of the particles inside the cell are out of focus. An image captured for diluted blood sample is shown in Figure 21. For this image, the blood sample has been put in a constant magnetic field for more than 10 hours (a permanent magnet is used in this case instead of the pulse field). Some signs of clustering can be observed in the image but most of the cells are out of focus. In free running mode of the camera, all things are moving since it is a liquid environment. Cells can be observed moving into and out of the object plane constantly. The situation of nanoparticle suspension is similar but smaller in scale since

nanoparticles are much smaller in size compared with blood cells. To reach higher imaging quality, special cells of short length ( $\sim 50\mu\text{m}$ ) should be prepared so that particles or cells can be confined within the depth of focus.

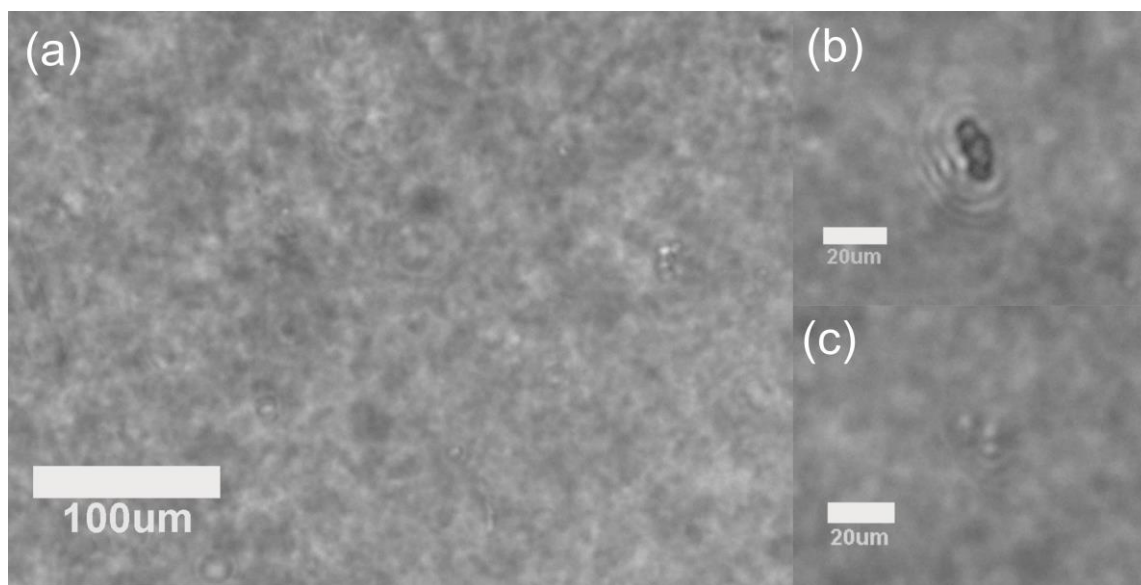


*Figure 21. Images Captured for Diluted Blood Sample: possible clusters and chains of bloodcells are found in (a), (b) and (c)*

Although, in Figure 21, most cells are out of focus, their location is can be more accurately located. When a cell is out of focus, a circle shaped diffraction pattern is captured instead. Assuming that the location of the cell is at the center of the diffraction center, their in-plane location and speed can be easily detected. If their off-plane distances can be calculated from the diffraction pattern, their speed inside the liquid can be directly determined. As particles or cells move into and out of the object plane, statistical information about their movement speed can be collected. Our purpose here is to show that while not optimized, this is within the present capability of the system. A research project dealing with scattering and aggregation in blood subjected to magnetic fields is expected to start in the near future.



Another interesting area of investigation would be that of interfaces and boundaries between magnetic and non-magnetic materials in thin film samples, and how these boundaries might change as the samples are annealed. The obvious problem with thin film samples with strong magnetic response is that of light throughput, as these samples tend to be opaque. For such cases, it would be desirable to modify the system to work in reflection geometry, and in the presence of a garnet film that acts as a Faraday indicator <sup>[4]</sup>.

## 7.2 Possible Improvements for the System

The system is shown to be in working state currently but there are still many aspects where it can be improved.

Better solutions should be developed to deal with the vibration problem described in Section 5.2. a more stable sample holder would prevent movement of the sample during the magnetic pulse. Since currently the objective must be inserted into the solenoid to view the sample at the middle, the objective can be also affected by the pulse field. To reduce any disturbance to the objective, the length of the solenoid can be reduced so that the objective can remain outside the solenoid. Moreover, for small vibrations, digital image stabilization techniques can be developed to further clean up the image. The ideal solution for this problem will likely be a mixture of hardware and software approaches.

The current solenoid used right now can provide a magnetic pulse field with a peak value of proximately 0.5T. For a phenomenon that requires higher field, the solenoid would need to be redesigned to provide bigger pulse field.

To improve the resolution of the imaging system, the spherical tube lens can be replaced by a standard tube lens compatible with the objective. This change is straight forward and can also lead to significant improvements in resolution.

The white light source used right now has a very broad bandwidth. For applications where responses for different wavelengths are investigated, this light source is very useful but a spectrometer is still needed to be constructed to realize these applications. Since a laser is not suitable for wide field imaging due to its coherence as discussed in previous chapters, for applications where the wavelength is specified, using arc lamps such as mercury or xenon lamp with band filters is a good solution to this problem. A strong arc lamp with good collimation can also increase the light throughput of the imaging system, thus improving its sensitivity.

## REFERENCE

- [1] Zhao, X. R., et al. "Magneto-optical imaging for high-throughput characterization of combinatorial magnetic thin films." *Applied surface science* 223.1 (2004): 73-77.
- [2] Suwa, Masayori, et al. "Faraday rotation dispersion microscopy imaging of diamagnetic and chiral liquids with pulsed magnetic field." *Analytical chemistry* 85.10 (2013): 5176-5183.
- [3] Murakami, Hironaru, Iwao Kawayama, and Masayoshi Tonouchi. "Fabrication of a prototype laser-magneto-optical imaging system." *Physica C: Superconductivity* 460 (2007): 1489-1490.
- [4] Murakami, Hironaru, and Masayoshi Tonouchi. "High-sensitive scanning laser magneto-optical imaging system." *Review of Scientific Instruments* 81.1 (2010): 013701.
- [5] Jackson, John David. *Classical Electrodynamics*, 3rd edition. John Wiley & Sons, 1999, pp. 316-319.
- [6] Gåsvik, Kjell J. *Optical Metrology*. John Wiley & Sons, 2003.
- [7] Pedrotti, Frank L., and Leno S. Pedrotti. *Introduction to Optics*, 2nd edition. New Jersey: Prentice Hall, 1993, pp. 247-265.
- [8] Goodman, Joseph W. *Introduction to Fourier optics*, third edition. Roberts and Company Publishers, 2005.
- [9] Gonzalez, Rafael C., and Richard E. Woods. *Digital Image Processing*, 3rd edition. Pearson Education Inc., 2005, pp. 213-219.
- [10] Thomas Foulkes, "Probing magnetization dynamics with pulse magnetic fields.", Rose-Hulman Institute of Technology, 2015
- [11] Courjon, Daniel, and C. Bainier. "Near field microscopy and near field optics." *Reports on progress in Physics* 57.10 (1994): 989.

[12] Darras, A., et al. "Relating Brownian motion to diffusion with superparamagnetic colloids." *American Journal of Physics* 85.4 (2017): 265-270.

[13] Li, Jian, et al. "Coordinated chain motion resulting in intensity variation of light transmitted through ferrofluid film." *Physics Letters A* 372.46 (2008): 6952-6955.

[14] Tao, R., and Ke Huang. "Reducing blood viscosity with magnetic fields." *Physical Review E* 84.1 (2011): 011905.

## APPENDIX 1. FINAL SETUP DETAIL

The figure below shows a detailed vertical view of the final setup. The optical components and mounts are drawn in black outlines as they are generally aligned at the same height (about 15cm). The parts with grey outlines are posts, holders, base plates or translation stage. The red line indicates the light path of He-Ne laser while the green line indicates the light path of white light. Each indexed component is described in the following section.

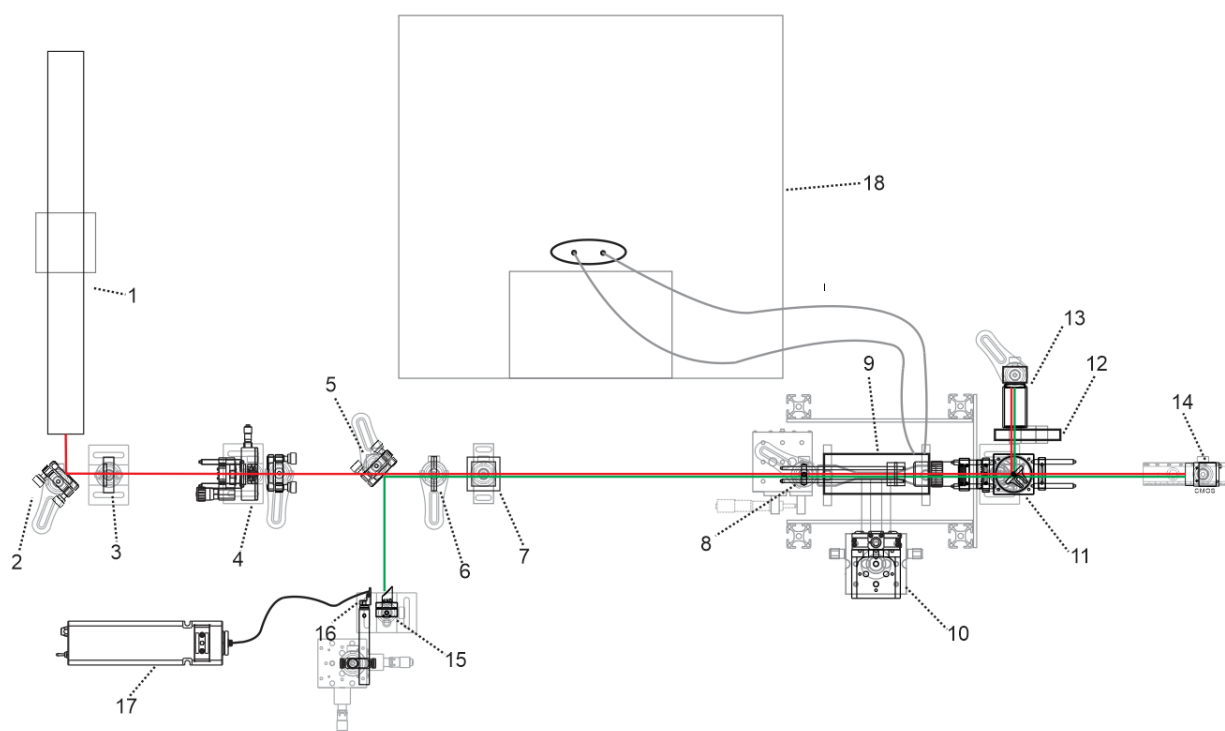


*Figure 22. Vertical View of Final Setup*

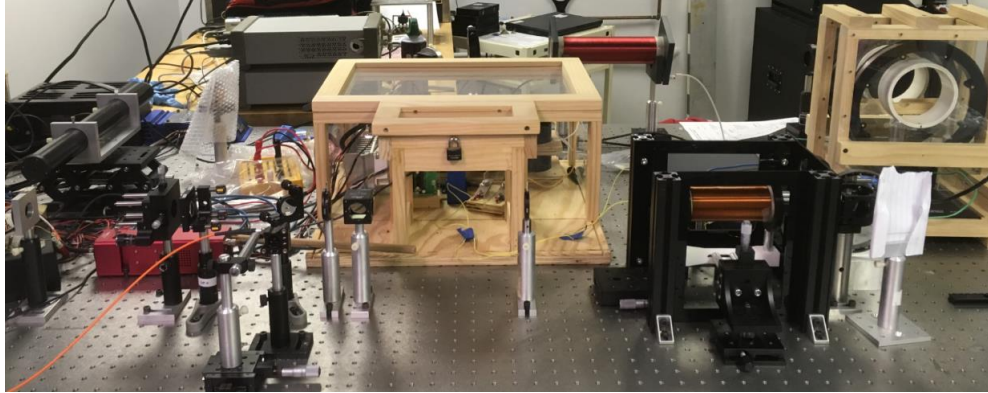


*Figure 23. Photograph of Final Setup*

1. He-Ne Laser

Model: Melles Griot 25-LHP-991 (632.8nm)

Beam diameter ( $1/e^2$ ): 0.65mm

Power: 10mW

Divergence: 1.24mrad

2. Protected Silver Mirror

Model: Thorlabs PF10-03-P01

3. Polarizer

Model: PASCO (unknown model)

Comment: This polarizer is only used for intensity control.

4. Spatial Filter

The spatial filter consists of three optical components as shown in the figure below:

(1) Aspheric Lens

Model: Thorlabs A397TM-B

Focal Length: 11mm

Anti-Reflective Coating: 650-1050nm

(2) Pinhole

Model: Thorlabs P20S

Diameter: 20um

(3) Plano-Convex Lens

Model: Thorlabs LA1422-B

Focal Length: 40mm

Material: N-BK7

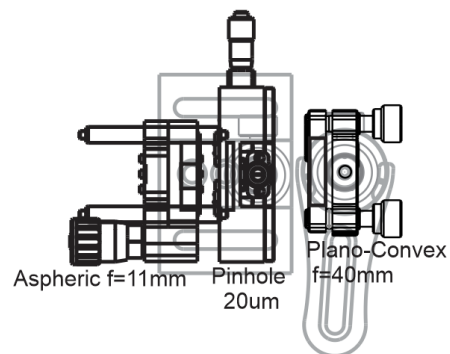


*Figure 24. Vertical View of Spatial filter*

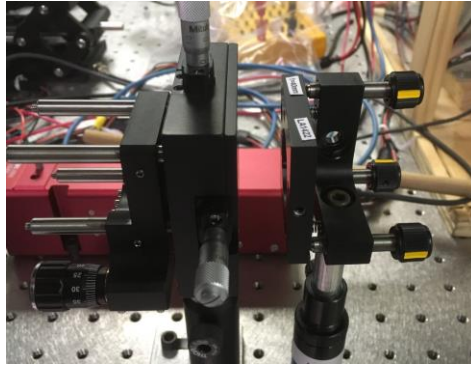


*Figure 25. Photograph of Spatial Filter*

5. Protected Silver Mirror

Model: Thorlabs PF10-03-P01

Comment: This mirror is mounted on a flip mount adapter so quick changes can be made between laser light and white light source.

6. Iris

Model: Thorlabs ID25Z

Comment: This iris is used to block some of the high-order beams that pass the spatial filter to reduce interference with the zero-order beam caused by aberration.

7. Polarizing Beam Splitter

Model: Thorlabs

Comment: Light is linearly polarized at the input of the system.

8. Rail for Sample Holder



Comment: This mechanical part is used to support the sample holder and isolate the sample from the solenoid to avoid vibration during measurements.



*Figure 26. Rail for Sample Holder*

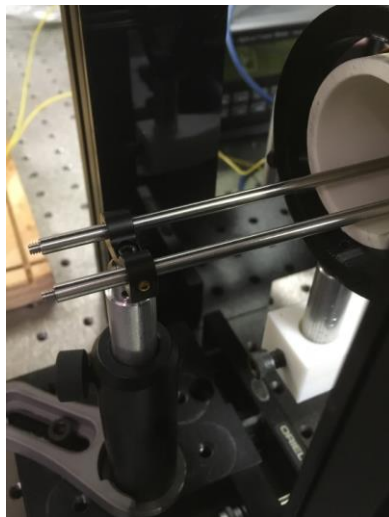


*Figure 27. Photograph of Sample Holder*

## 9. Solenoid

Material: copper

Parameters: 610 turns and 4 layers

Resistance:  $\sim 5.2\text{ohm}$

Comment: The solenoid is mounted inside the capacitor bank system as shown in Figure 28 and aligned with the light path. Detailed description about the solenoid load can be found in Thomas Foulkes's paper<sup>[10]</sup>.

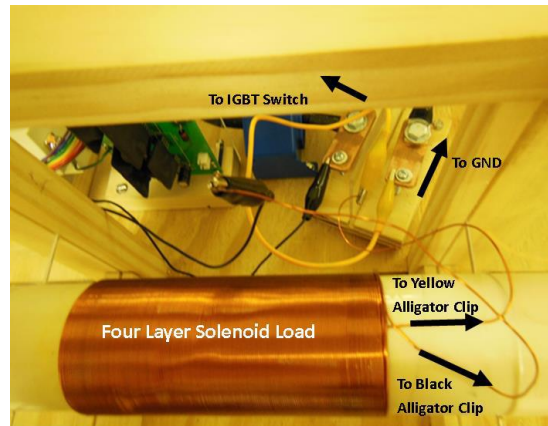


Figure 28. Solenoid and its connection<sup>[10]</sup>

## 10. Translation Stages

Model: Thorlabs MT1

Comment: The combination of two one-axis stages provides a two-axis field of view adjustment. The holder for the solenoid is connected to the stages.

## 11. Microscope

The microscope consists of three optical components as shown in the figure below.

### (1) Objective

Model: Mitutoyo MY10X-803

Magnification: 10X

Type: apochromatic and infinity corrected

Working Distance: 34mm

### (2) Polarizer

Model: Newport 10LP-VIS

Wavelength Range: 430-670nm

Extinction Ratio: 4000:1

Comment: This polarizer is 45 degree with respect to the one before.

### (3) Beam Splitter

Model: Thorlabs BSW10

Split Ratio: 50:50

Wavelength Range: 400-700nm

### (4) Plano-Convex Lens

Model: Thorlabs LA1253

Focal Length: 200mm

Material: N-BK7

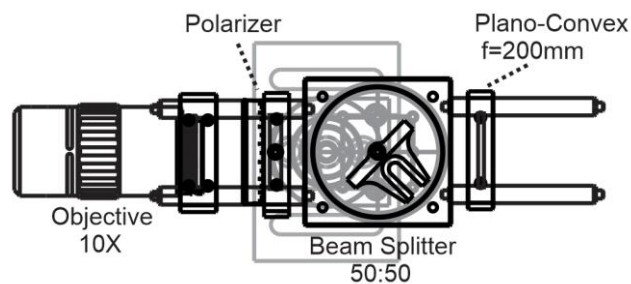


*Figure 29. Vertical View of Microscope*

### 12. Metallic Wheel Filter

Comment: The wheel as shown in Figure 30 is used to adjust the input intensity to the power meter.

### 13. Photodetector

Model: Newport 818-SL

Comment: The power meter is connected to an oscilloscope to monitor light intensity changes.

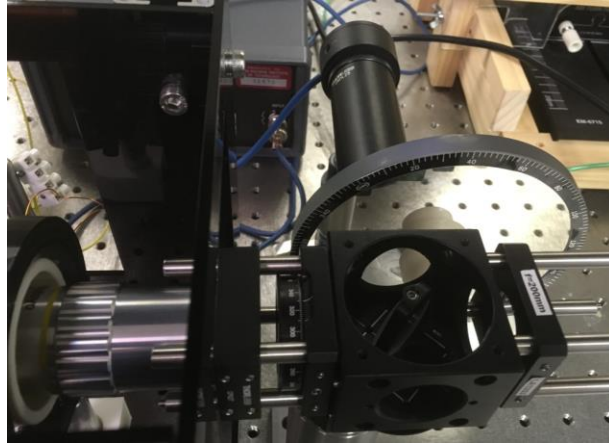


*Figure 30. Photograph of Microscope, Metallic Wheel Filter and Photodetector*

#### 14. Camera

Model: Point Grey GS3-U3-51S5M-C

Comment: The camera is mounted on an optical rail so that movement along the optical path can be made easily. The camera settings are generally adjustable for different applications so detailed parameters will be listed for specific measurements.

#### 15. Silver Parabolic Mirror

Model: Thorlabs OAP MPD00M9-P01

Comment: The off-axis parabolic mirror is used to collimate the white light from a fiber without introducing any chromatic aberration.

#### 16. Fiber Clamp

Model: Thorlabs FCM32

Comment: The clamp is connected to a two-axis translation stage to help adjust the location of the fiber.

### 17. White Light Source

Model: Thorlabs SLS201 (coupled with S120-SMA fiber)

Bandwidth: 360-2600nm

Coupled power: >10mW

### 18. Capacitor Bank (pulse generator)

The capacitor bank stores energy and generate pulse current into the solenoid. The main system is described in Thomas Foulkes's paper<sup>[10]</sup>. The amplitude and the duration of the magnetic pulse field generated by the capacitor bank depend on the voltage applied on the solenoid and their relation is described in Section 6.1.

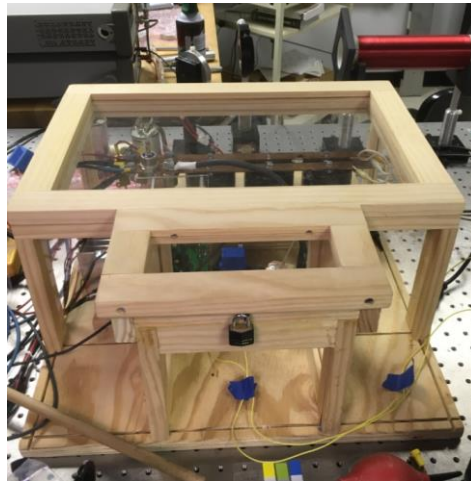


*Figure 31. The Capacitor Bank*

## APPENDIX 2. PRELIMINARY SETUP DETAIL

Similar to Figure 22, the figure below shows a detailed vertical view of the preliminary setup. Some of parts are also used in the final setup, so the description of those parts will only refer to the corresponding part in Appendix 1 to save writing space.

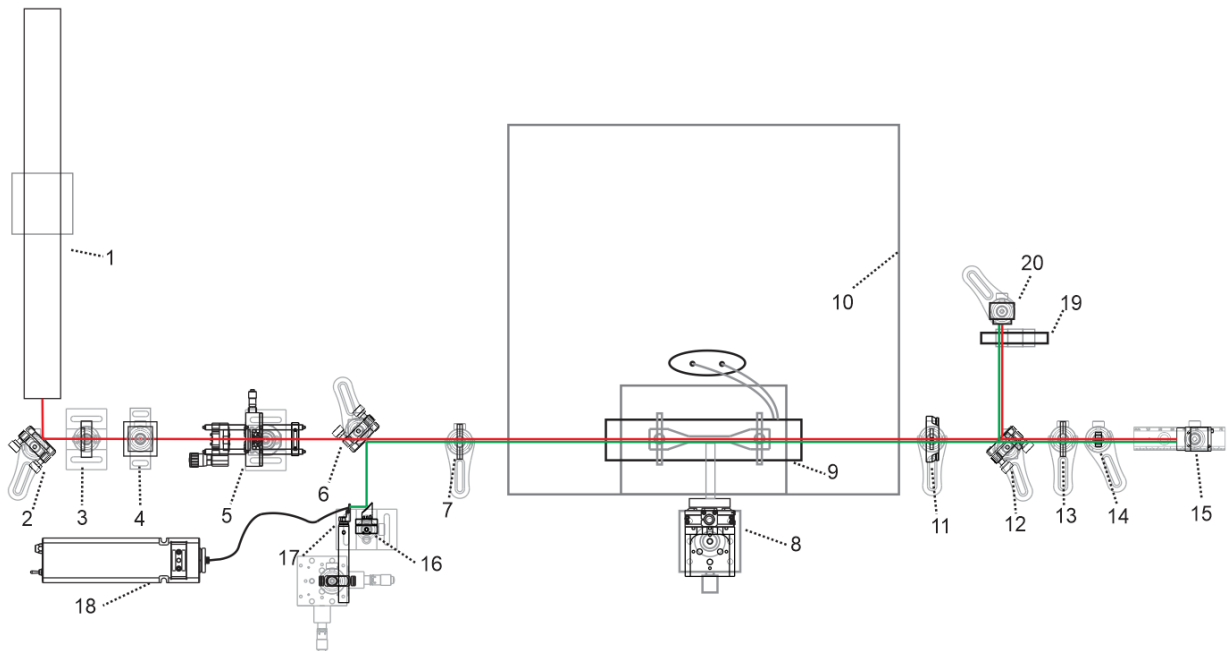


*Figure 32. Vertical View of Preliminary Setup*

1. He-Ne Laser

Reference: Appendix 1 Part No. 1

2. Protected Silver Mirror

Reference: Appendix 1 Part No. 2

3. Polarizer

Reference: Appendix 1 Part No. 3

4. Polarizing Beam Splitter

Reference: Appendix 1 Part No. 7

5. Spatial Filter

Reference: Appendix 1 Part No. 4

6. Protected Silver Mirror

Reference: Appendix 1 Part No. 5

7. Iris

Reference: Appendix 1 Part No. 6

8. Translation Stages

Reference: Appendix 1 Part No. 10

9. Solenoid

Reference: Appendix 1 Part No. 9

10. Capacitor Bank (pulse generator)

Reference: Appendix 1 Part No. 18

#### 11. Polarizer

Reference: Appendix 1 Part No. 11 (2)

#### 12. Protected Silver Mirror

Model: Thorlabs PF10-03-P01

Comment: This mirror is mounted on a flip mount adapter to make quick changes between imaging detector and power meter.

#### 13. Iris

Model: Thorlabs ID25Z

Comment: This iris is used to control the input beam size to the concave lens since large aperture size could result in more aberration and diffraction patterns.

#### 14. Plano-Concave Lens

Model: Thorlabs LC2969

Material: N-SF11 (uncoated)

Focal length: -6mm

Comment: The concave lens is used to diverge the beam and enlarge the image.

#### 15. Camera

Reference: Appendix 1 Part No. 14



16. Silver Parabolic Mirror

Reference: Appendix 1 Part No. 15

17. Fiber Clamp

Reference: Appendix 1 Part No. 16

18. White Light Source

Reference: Appendix 1 Part No. 17

19. Metallic Wheel Filter

Reference: Appendix 1 Part No. 12

20. Photodetector

Reference: Appendix 1 Part No. 13

### APPENDIX 3. HARDWARE INTEGRATION USING LABVIEW

Since the experimental setup includes multiple controls (voltage control and pulse trigger) and detectors (photodetector and digital camera), Labview interfaces and programs integrating all hardware are developed to enable easier user control and automatic measurements. Currently, Labview interfaces for pulse triggering mechanics, oscilloscope and digital camera are built and tested. The user interfaces are shown in following figures.

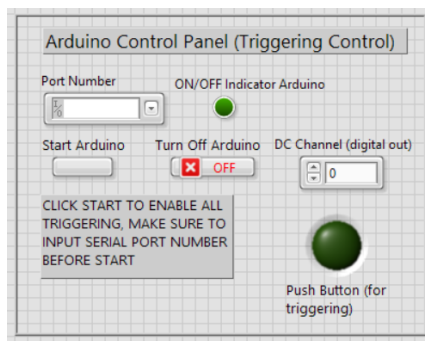


*Figure 33. User Interface for Pulse Triggering*

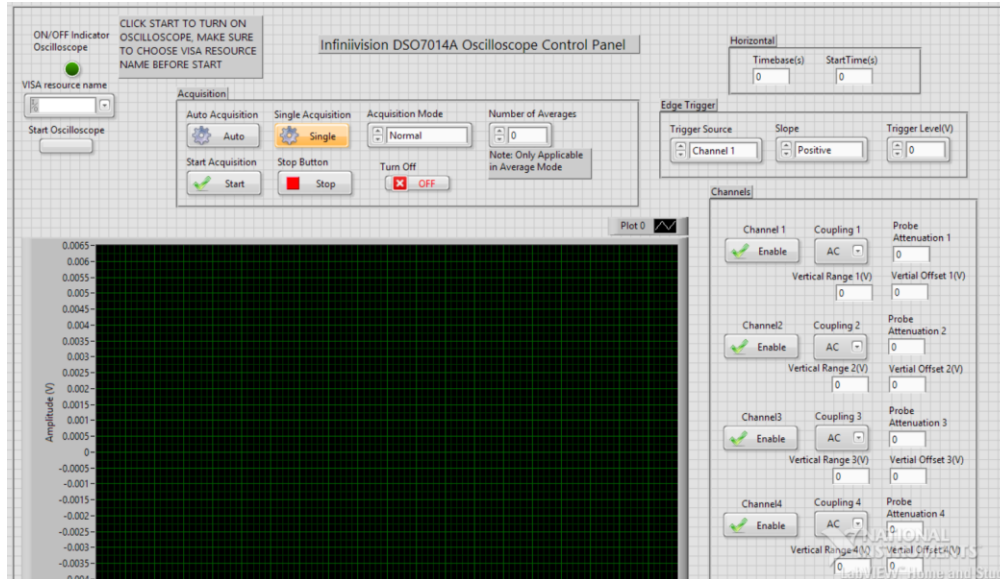


Figure 34. User Interface for Oscilloscope

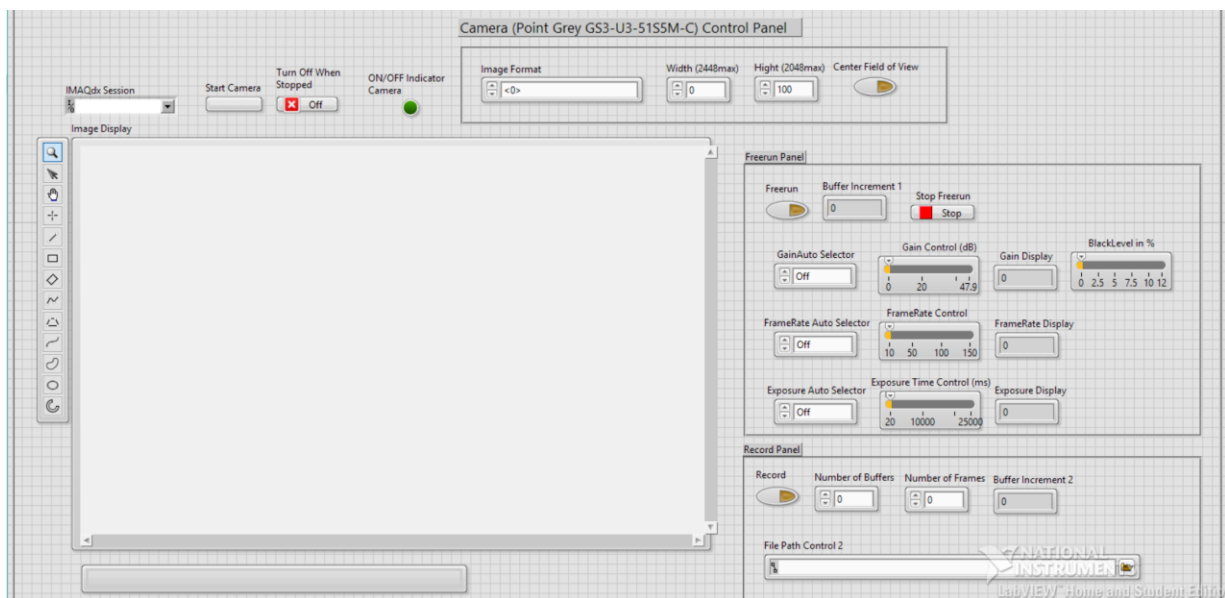
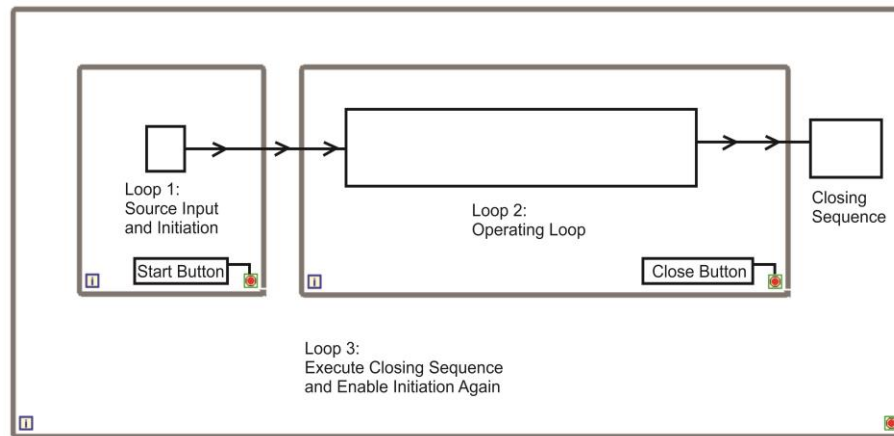


Figure 35. User Interface for CMOS Camera

The code behind those interfaces are similar in structure illustrated in Figure 36. After the program is started, the program will be running within Loop 1, at the same time waiting for the source input and initiation. A start button is used to start the initiation and end Loop 1. Then Loop

2 is executed and all functioning of the interface is enabled. After all the operations, clicking the close button can initiate the closing sequence to close the hardware. Because of the presence of Loop3, Loop 1 will start again and wait for the next initiation. Loop 3 enables the user to close and start the hardware without closing the whole program. This structure aims to enable all hardware to work separately or together in the same VI (Visual Instrument). A simple example of this structure is shown in Figure 37 which is the code for pulse triggering. The code for the oscilloscope and camera are much more complicated and occupy large space because of the graphic nature of programming in Labview, so it is omitted in this appendix.



*Figure 36. Structure of the Code*

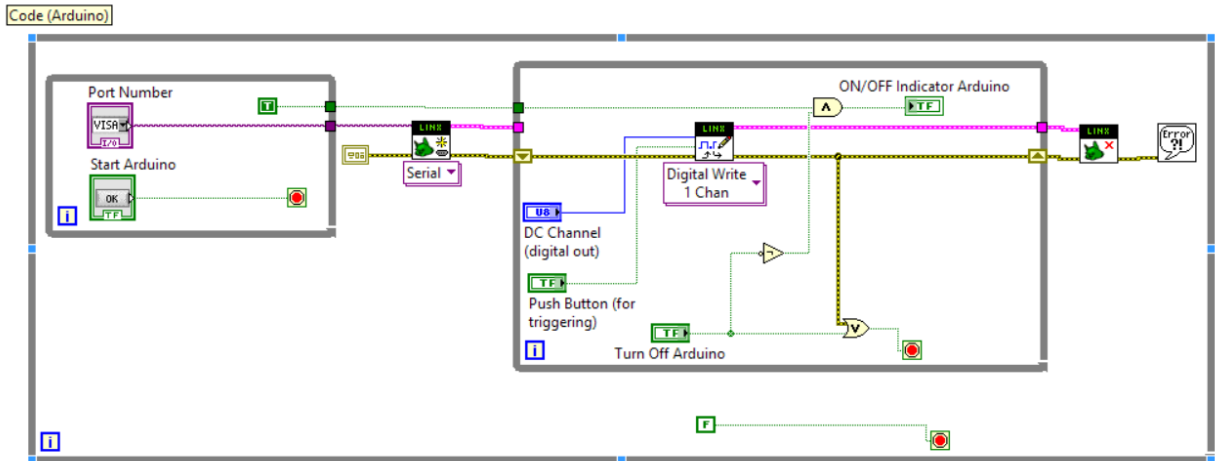


Figure 37. Code for Pulse Triggering

The interfaces make it easier to remotely control all the hardware. More importantly, because all the drivers and functionalities have been tested, the code serve as examples for more integrated programs. A program for automatic multiple measurements has been written based on the code of those interfaces. The front panel of the program is shown in Figure 38.

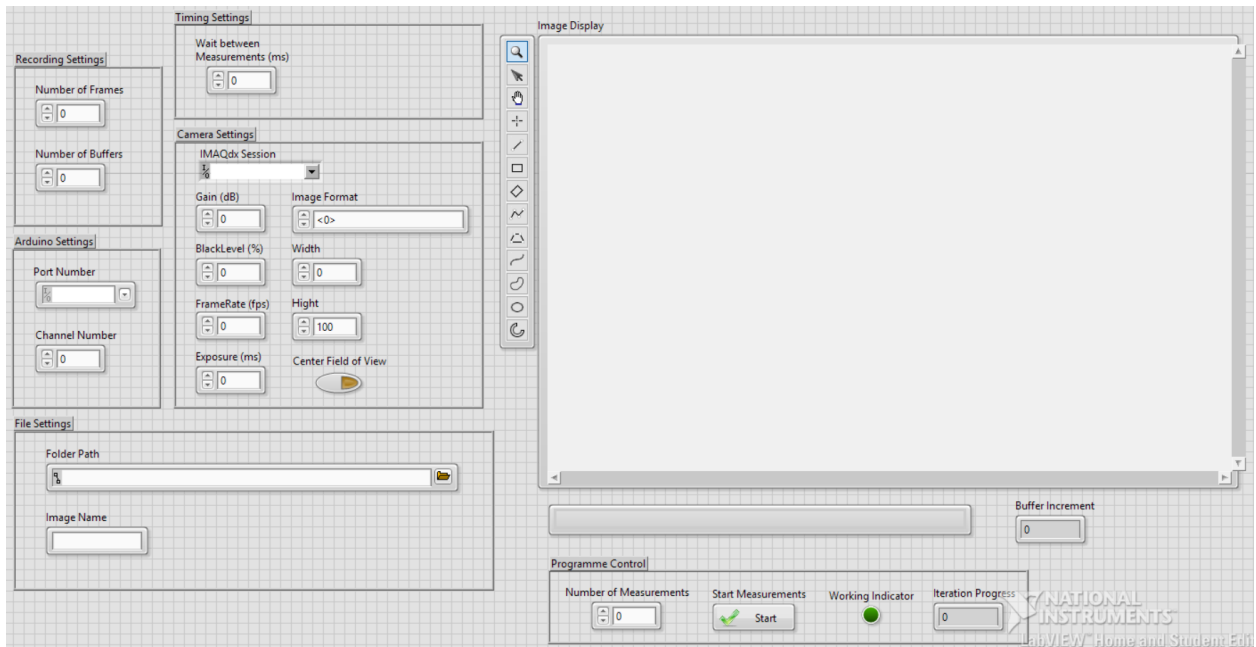


Figure 38. Front Panel of the Program for Auto-Measurements

The purpose of this program is to do scheduled measurements automatically for an extended period. The general procedure of the program is illustrated in the Figure 39. Assuming the sample does not change its respond to magnetic field and light, the results from multiple measurements can be added together to enhance signal to noise ratio.

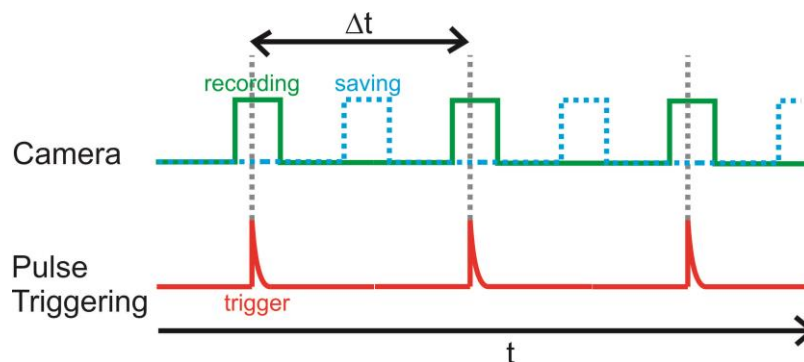


Figure 39. Program Procedure for Multiple Auto-Measurements

As shown in Figure 39, multiple measurements can be scheduled and processed automatically. The time between two measurements,  $\Delta t$ , can be adjusted to avoid the solenoid heated up and give time for file saving and program initiation. The pulse is fired in the middle of a recording so images from both before and after the pulse are recorded for further processing.

## APPENDIX 4. MECHANICAL PARTS

In order to construct the system and enable more flexibility, some customized parts are made and will be described in this appendix. All parts are designed in SolidWorks and 3D printed with hard plastic.

### 1. Sample Holder

This holder is designed to fix and hold a thin film sample with a about one by one inch size. The sample is fixed by an 8-32 plastic screw. The holder can be fixed on two rods from Thorlabs 16mm cage system (model: SR6). The 3D model of the holder is shown in Figure 40.

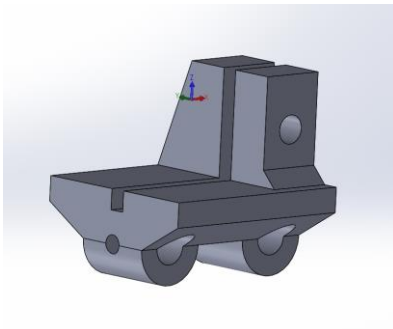


*Figure 40. Sample Holder (3D model)*



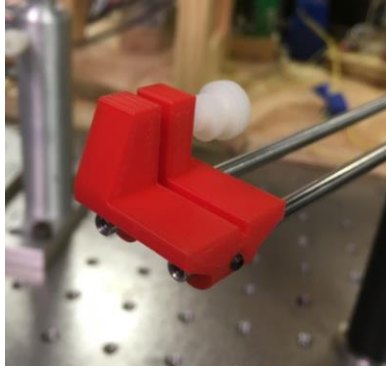


*Figure 41. Photograph of the Sample Holder*

## 2. Solenoid Mounts

In the final setup, the solenoid is constrained in two adjustable mounts as shown in Figure 42. The solenoid is fixed by three 8-32 screws inserted through the mounts. These mounts are also used to reduce possible vibration of the solenoid caused by the strong magnetic pulse field.

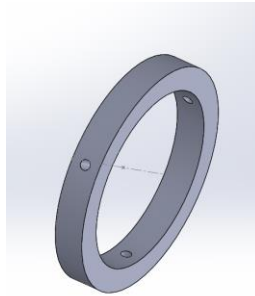


*Figure 42. Solenoid Mount (3D model)*

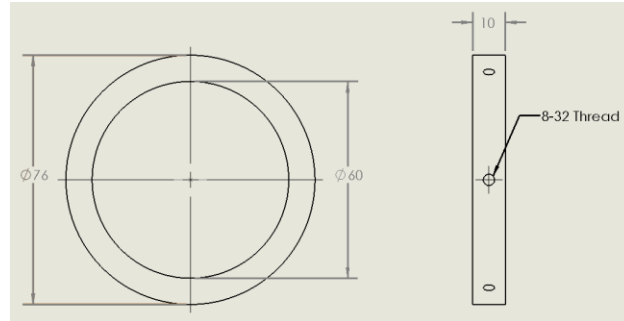


*Figure 43. Drawings of the Solenoid Mount*

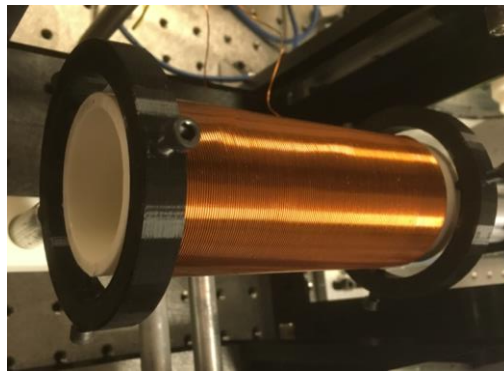


*Figure 44. Photograph of the Solenoid Mounts*

### 3. Solenoid Holder

This holder is designed to connect the solenoid to a two-axis transition stage to enable transverse adjustment. The 3D model of the part is shown in Figure 45 and a photograph of the part in the real system is shown in Figure 47.

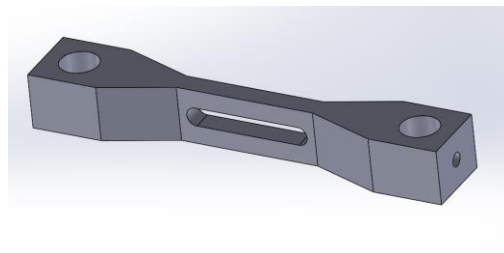


*Figure 45. Solenoid Holder (3D model)*

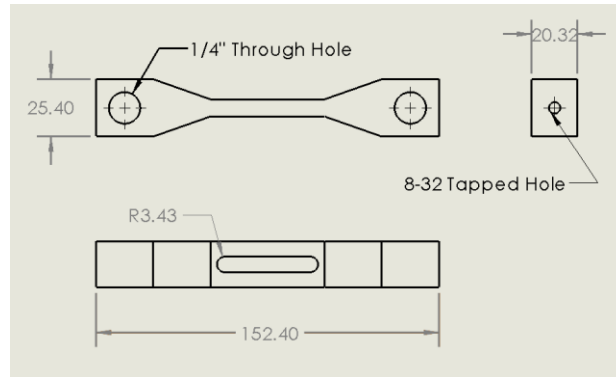


*Figure 46. Drawings of the Solenoid Holder*

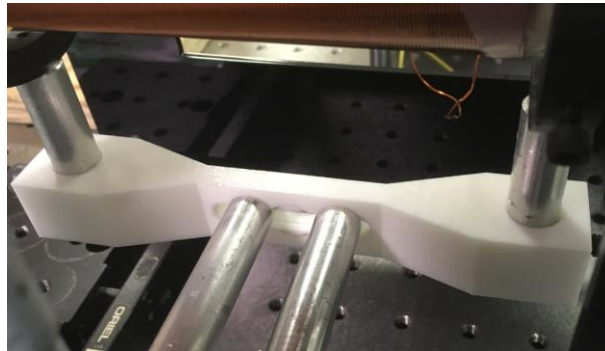


*Figure 47. Photograph of the Solenoid Holder*

#### 4. Solenoid Housing

A customizable housing is designed for the solenoid for safety concern. The housing should be able to reduce unnecessary contact between the solenoid and other external components and hands. The housing consists of four plastic plates connected by 30x30mm aluminum extrusions. Big openings on each plate prevent any mechanical interference and allow maximum adjustment to the system. The housing can also be fixed onto the optical table by using 90 degree brackets.

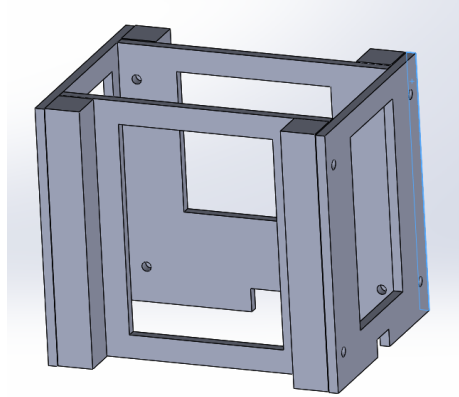


*Figure 48. Solenoid Housing (3D model)*

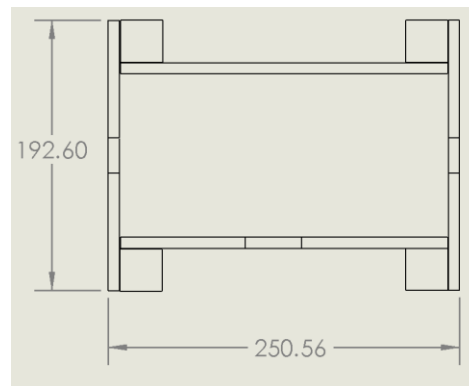


*Figure 49. Drawing of the Solenoid Housing*

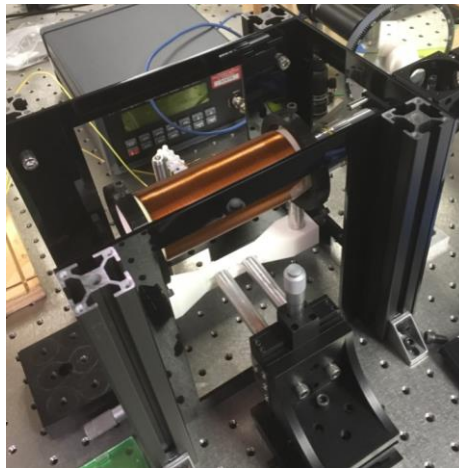


*Figure 50. Photograph of the Solenoid Housing*

## **APPENDIX 5 DEPOSITION PROCESS**

A metal film is prepared in the MiNDS lab (Micro-Nano Device and Systems) for testing purpose. The substrate of the film is a cover glass (company: Corning; size: 22x22mm; thickness: 0.12-0.16mm). The glass substrate is thin enough so that its contribution to the total magnetic response can be neglected. The process is illustrated in Figure 51. The cover glass is firstly taped on a dummy wafer. Then, another cover glass is taped on top of the first one and cover half of the area as shown in the step 2 of Figure 51. The wafer is then put in the Vapor Deposition System (PVD75, Kurt J. Lesker) to deposit a 50nm thick nickel film. After the first deposition, the second deposition of aluminum using the Sputtering Deposition System is conducted with the other half of the area covered. Because of the limited precision, there is a small area where nickel and aluminum overlap as shown in the final result of Figure 51.

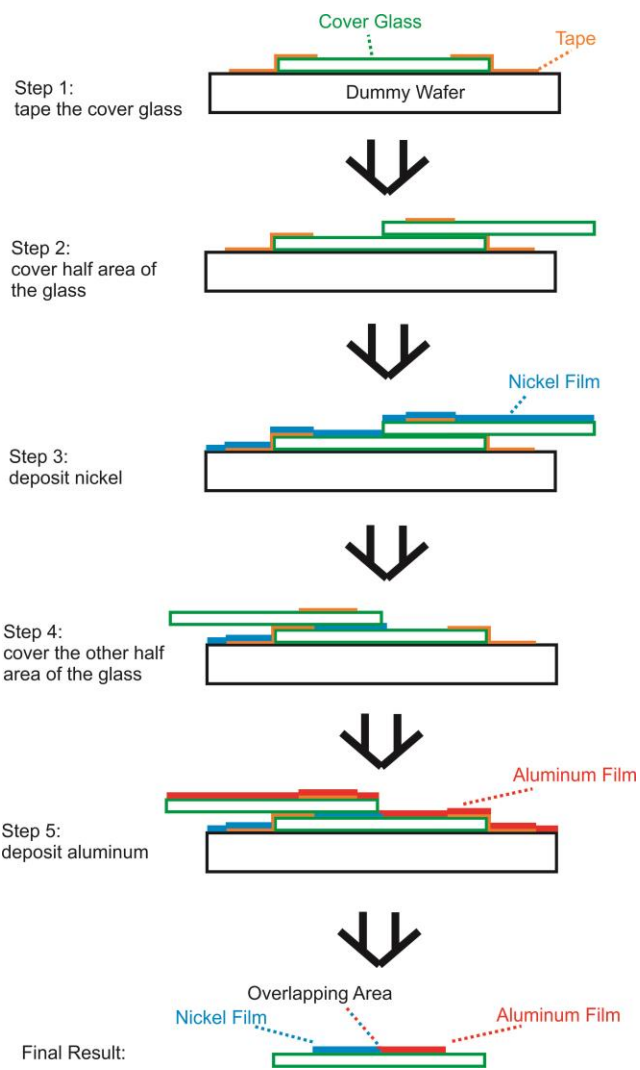


Figure 51. Schematic of Deposition Process